Response of zirconium - 1.5%Sn to autogenous gas tungsten arc welding

by

Njingalwazi Magwentshu

Submitted in partial fulfillment of the requirements for the degree

Master of Engineering

in the Faculty of Engineering, the Built Environment and Information

Technology, University of Pretoria

January 2018

ABSTRACT

The influence of heat input on the as-welded microstructure and hardness of autogenous bead-on-plate gas tungsten arc welds on nuclear grade Zircaloy-2 was investigated. In addition, the β-α transformation behaviour was examined using dilatometry. In particular, the transformation start and transformation end temperatures at various cooling rates were determined.

The microstructure of the welded joints (heat input 10 to 90 J/mm) and of the dilatometry samples (at cooling rates of 600 to1.1°C/s) was predominately basket-weave. In the range of cooling rates used, the hardness did not change with the fraction basket-weave structure or the prior beta grain size. The hardness of the weld metal and heat affected zone was not sensitive to heat input or the use of a pulsed power supply for the range of heat input and welding speed investigated. There was no difference in hardness between contaminated welds and non-contaminated welds. Second phase particles found in the base material did not seem to be present in the weld metal or HAZ .

The transformation start and transformation finish temperatures, on heating, for all the samples were 807°C to 1071°C. On cooling, transformation start and transformation end range was 801°C to 647°C. The cooling time from 900$^{\mathbf{o}}$C to 600$^{\mathbf{o}}$C, $\Delta t_{\text{9-6}}$, calculated for weld metal and HAZ was therefore considered an appropriate parameter.

The findings show that Zircaloy- 2 has good weldability over wide range parameters and that practical welding problems such as shielding did not compromise the integrity of the welds.

Keywords: Zircaloy-2, GTAW, Alpha phase, Beta phase, Phase transformation.

TABLE OF CONTENTS

ACKNOWLEDGEMENTS

List of Tables

List of Figures

List of Equations

Chapter 1: Background and outline of study

1.1 Introduction

Zirconium is a metallic material which finds most of its applications in the nuclear industry and in severely corrosive applications in the chemical processing industry[1]. Welding of zirconium alloy components is one of the most critical steps during the manufacturing of nuclear reactor fuel elements. In the chemical processing industry, small amounts of contamination resulting from inadequate cleanliness or from poor atmospheric control during welding may lead to diminished corrosion resistance of the weld and, in severe cases, to weld failure.[2]

1.2 Problem statement

The purpose of this study was to investigate the as-welded microstructure and hardness of an autogenous bead-on-plate gas tungsten arc weld for nuclear grade zirconium 1.5%Sn. In addition, the β-α transformation behaviour during cooling was examined, using dilatometry.

The following experimental techniques were used:

- Autogenous gas tungsten arc welding (GTAW).
- An analysis of the influence of heat input on the as-welded microstructure of the weld metal and the heat affected zone, using optical metallography.
- Dilatometry to evaluate the transformation behaviour under a range of cooling rates that varied from about 1.1°C/s to 600°C/s. These cooling rates represent a similar range of cooling rates to those estimated for the gas tungsten arc welds done during this study.
- Hardness tests on the weld bead, heat affected zone and dilatometry samples.

1.3 Outline of the study

Autogenous gas tungsten arc welding (GTAW) was used to weld zirconium 1.5%Sn sheets with a nominal thickness of 1.2 mm. Argon was used in the welding torch, the trailing gas shield and as a backing gas. The heat input and cooling rate of the weld was calculated from the width of the weld bead using the Rosenthal equation for thin plate.

Dilatometry was used to investigate the phase transformation of zirconium 1.5%Sn during heating to a range of peak temperatures and subsequent cooling at various rates. The heating rate was 100^0C/s. The peak temperatures investigated were 900°C and 1100°C. The cooling rate for the 900°C peak temperature was 0.9°C/s, 9°C/s and 90°C/s. For the 1100°C peak temperature, the cooling rate was 1.1°C/s, 11°C/s, 50°C/s, 110°C/s, 300°C/s and 600°C/s. Microstructures were analysed using an optical microscope.

Hardness measurements were done for the dilatometry samples and welded samples. The hardness of the base metal, weld metal and the HAZ differ by less than 20 HV 0.3.

Chapter 2: Overview of zirconium alloys

2.1 Overview

Zirconium has been studied for industrial use in nuclear energy for more than seven decades. Parameters of nuclear reactors like; burn up, neutron flux density, neutron spectrum and temperature have a significant impact on the reactor core elements. The welding of fuel rods is essential in ensuring the reliability of nuclear reactors. The number of fuel rods with fabrication defects of welded joints is still far from the desired zero value. The properties of the welds are determined by the presence of contamination, the residual stresses and quenching structures in welds and heat-affected zone (HAZ). These factors cause increased interest in the development of welding, brazing and soldering technologies of zirconium-based alloys that enable the formation of high quality joints.

Most studies focused on modernization of equipment and technology are used for welding end caps with fuel rods; gas tungsten arc welding in argon and helium, electron beam and resistance upset welding. Laser and resistance spot welding were used for manufacture of spacer grids. Friction and diffusion welding are sometimes used. Research on joining of zirconium alloys with other metals and alloys (such as stainless and carbon steels, hafnium, and Al-Fe-Ce alloys) continues[3].

2.1.1 Welding of zirconium overview

Gas tungsten arc welding

Gas tungsten arc welding of zirconium alloy components is often done in a welding chamber that can be evacuated to expel air and then backfilled with inert gas (argon, helium, or argon/helium mixtures. To minimize the risk of nitrogen contamination of fuel rods welds, the welding chamber is usually purged twice with an inert gas before the welding process. The quality features of gas tungsten arc welds are minimum leak path, no porosity and cracking. [18] In the past end caps of fuel rods were cladded using GTAW. In this particular study, bead on plate welds are to be done on 1.2mm thickness zirconium 1.5%Sn.

Electron beam welding

Electron beam welding is a fusion welding process in which a beam of high-velocity electrons is applied to the material being joined. The welding intensity may exceed 200 kW. The workpiece melt as the kinetic energy of the electrons is transformed into heat upon impact. The penetration of the electron beam lies between 0.1 and 1 mm. The welding is done in vacuum to prevent dispersion of the electron beam. This means that a shielding gas is not used. Contamination from the air is therefore eliminated. The rapid cooling of the weld pool may result in increased hardness of the fusion zone. A disadvantage of this welding process is the high capital investment cost of the equipment[18].

Laser beam welding

Nd YAG and CO_2 lasers are mainly used for welding application. Laser welding is normally carried out in air. Thus, both argon and helium separately or a mixture of both are used as the shielding gas. Due the low heat input, the microstructural change in the heat affected zone is very small. The short welding time suppresses any tendency for chemical reactions. Laser welding is high capital cost welding process[18].

2.2 Historical background

Zirconium was discovered in 1789. In 1949, zirconium was selected as a structural nuclear core and fuel clad material due to its combination of mechanical properties and low neutron absorption cross-section. In the 1960s, zirconium alloys became the main cladding material for water-cooled nuclear reactors. In the 1970s, the chemical process industry began to use zirconium in a variety of severely corrosive environments. Zirconium is currently available as nuclear and industrial grades[3].

2.3 Nuclear grades of zirconium

Nuclear grade or reactor grade zirconium is a hafnium-free alloy containing controlled impurity levels. Hafnium and boron levels in nuclear grade zirconium are less than 100 ppm. Pure nuclear grade zirconium is known as Grade R1 or Grade 21. Zircaloy is a series of zirconium-tin nuclear grade alloys containing minor amounts of iron, chromium and nickel [3].

Zircaloy grades are available in the following grades[3],[4]:

- Zircaloy-2: an alloy with the principal addition being tin (1.20-1.70%), with minor amounts of iron (0.07-0.2%), chromium (0.05-0.15%) and nickel (0.03-0.08%).
- Zircaloy-4: a variation of Zircaloy-2 with no nickel but with a higher iron content. Zircaloy-4 has a higher resistance to hydrogen pick-up during corrosion than Zircaloy-2.
- Grade R60814 and R60824: the same alloy as Zircaloy-4, with a lower oxygen content, to meet more stringent bend ductility requirements.
- Zr-2.5Nobium alloy: an alloy containing 2.5% nobium and 0.09% oxygen. The Zr-2.5Nb alloy was developed by Atomic Energy of Canada Limited (AECL) for the pressure tubes of CANDU reactor.

Table 1 shows the major alloying elements of various Zircaloy alloys.

2.4 Industrial grades of zirconium

Industrial grades of zirconium are manufactured using the Kroll process and contain naturally occurring levels of hafnium. The use of industrial grades, consequently, is limited to non-nuclear applications. The industrial grades include[3]:

- Technical grade: an unalloyed grade for metallurgical alloying. This grade is the least pure and is available only as a sponge metal. It is also known as Grade 703 or R60703.
- Commercial grade: zirconium that is not alloyed, specified for general corrosion-resistant service. It is also known as Grade 702, Grade II and R60702.

- Grade 704 (also known as R60704) is a zirconium-tin alloy based on the equivalent nuclear alloy. It is used in urea synthesis equipment and other chemical processes where the added strength of the alloy is required and the corrosion resistance is adequate.
- R60705: the industrial version of the Zr-2.5wt% niobium alloy used in some corrosion-resistant applications where high strength is needed.

Table 1: Chemical composition limit of nuclear grade and commercial zirconium alloys[(3),(4)]. Alloying content in %, except where otherwise stated.

Alloying elements	Nuclear grades			Commercial grades		
	Zircaloy-2	Zircaloy-4	Zr-2.5 Niobium	Grade 702	Grade704	R60705
Tin	1.20-1.70	1.20-1.70			1.00-2.00	
Iron	0.07-0.20	0.18-0.24		0.20 max	0.20-0.40	0.20 max
Chromium	0.05-0.15	0.07-0.13		0.20 max	0.20-0.40	0.20 max
Nickel	0.03-0.08					
Nobium			2.40-2.80			2.0-3.0
Oxygen	1400 ppm max	1400 ppm max	0.09-0.13			
Hafnium	100 ppm max	100 ppm max	100 ppm max	4.5 max	4.5 max	

2.5 The effect of alloying elements on the stability of α and β

Pure and zirconium alloys are present as α phase (hcp) at room temperature and β phase (bcc) at high temperatures. There are various alloying elements present in zirconium, as noted in the previous section, which are mostly added to improve the corrosion properties of the material. These alloying elements affect the α-β- transformation behaviour by stabilising either the α or β phase. The α-stabilising alloying elements increase the temperature for the transformation of α to β. Conversely, the stabilised β phase alloying elements decreases the temperature for the transformation of α to β. α-phase stabilizers include beryllium, cadmium, nitrogen, oxygen, pallidum and tin. β-phase stabilizers include cobalt, chromium, copper, iron, manganse, molybdenum, niobium, nickel, tantalum, thorium, titanium, uranium and tungsten[(1)].

The influence of α and β stabilisers on the transformation temperature can be understood by referring to a few selected phase diagrams. These phase diagrams were selected because tin, iron, nickel and chromium are intentional alloying elements in Zircaloy-2. Consider, for example, the zirconium-tin, zirconium-iron, zirconium-nickel, zirconium-chromium and zirconium- oxygen equilibrium phase diagrams (Figure 1 to Figure 5). Tin is an α stabiliser, while chromium, iron and nickel are all β stabilisers[1]. The role of the intermetallic compounds (Zr$_3$Fe, NiZr$_2$ and ZrCr$_2$) is discussed in the next session.
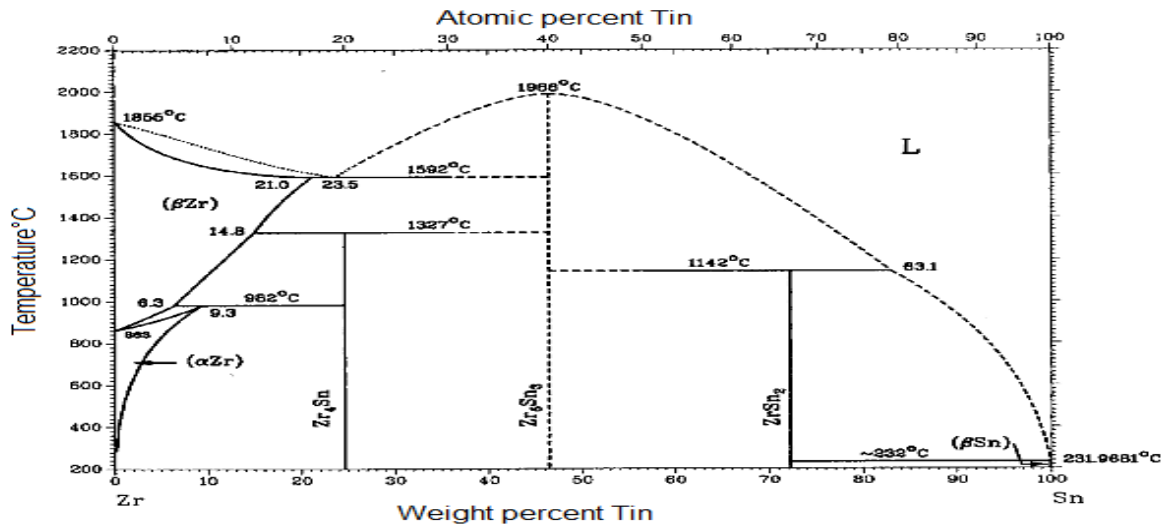
Figure 1: The zirconium - tin equilibrium phase diagram[1].
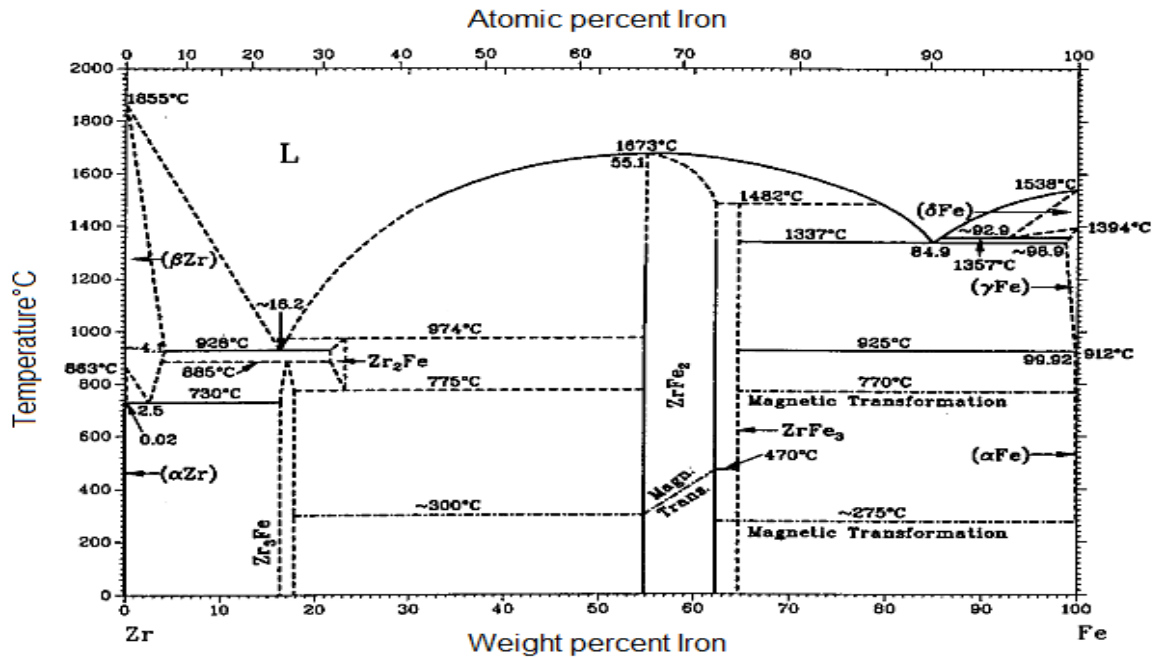
Figure 2: The zirconium - iron equilibrium phase diagram[1].
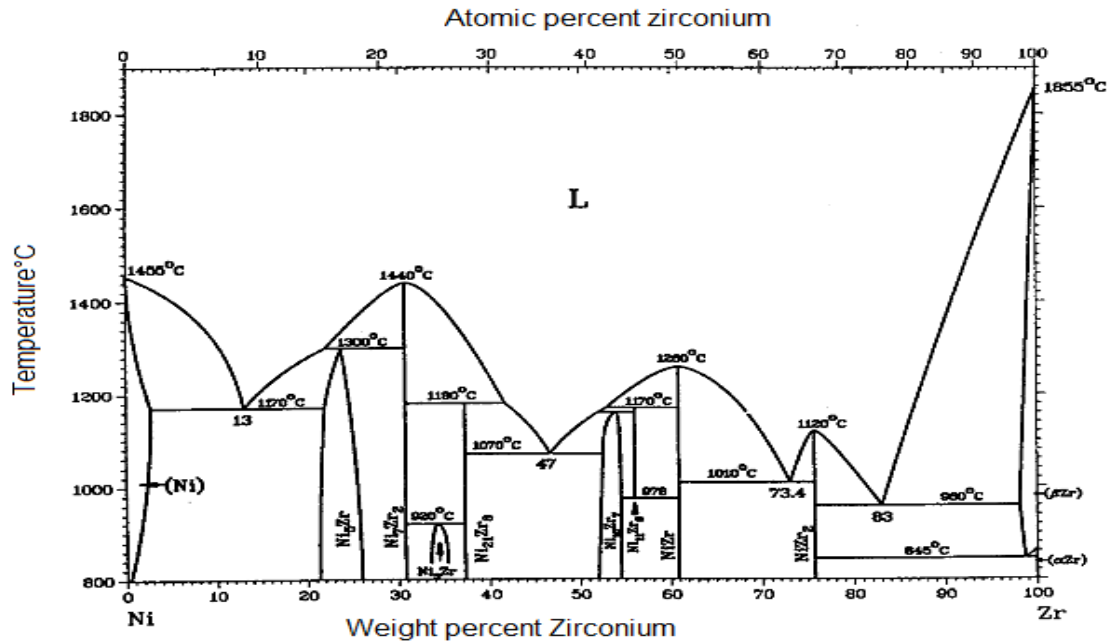
Figure 3: The zirconium - nickel equilibrium phase diagram[1].

18
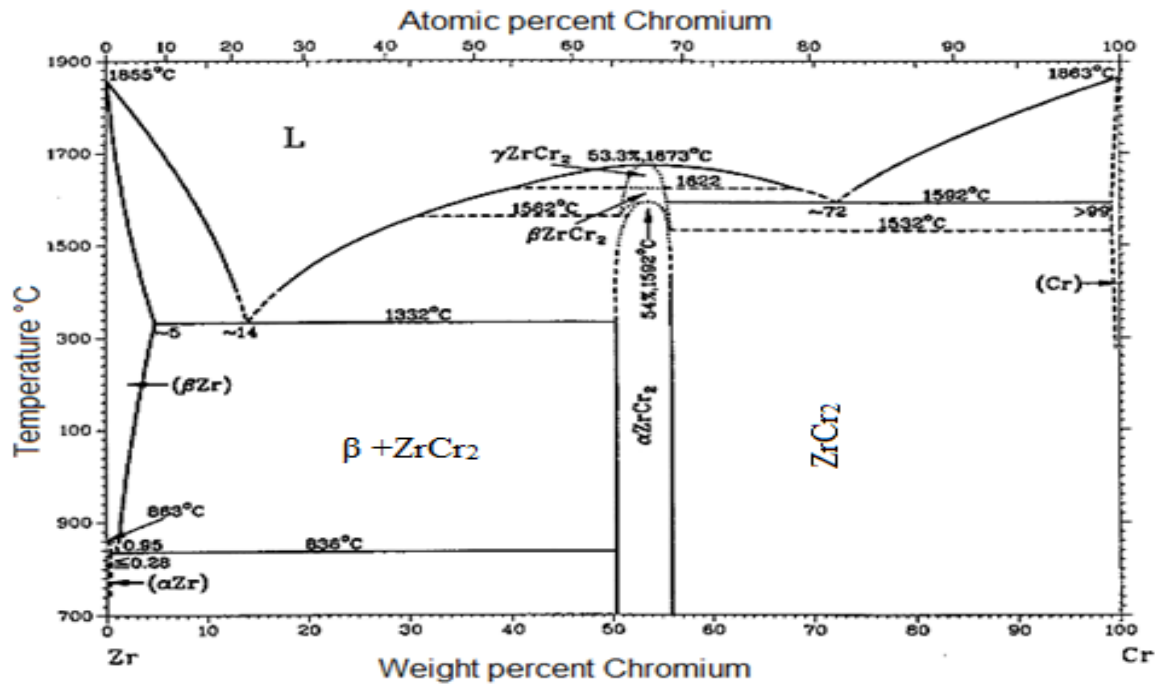
Figure 4: The zirconium – chromium equilibrium phase diagram[1].
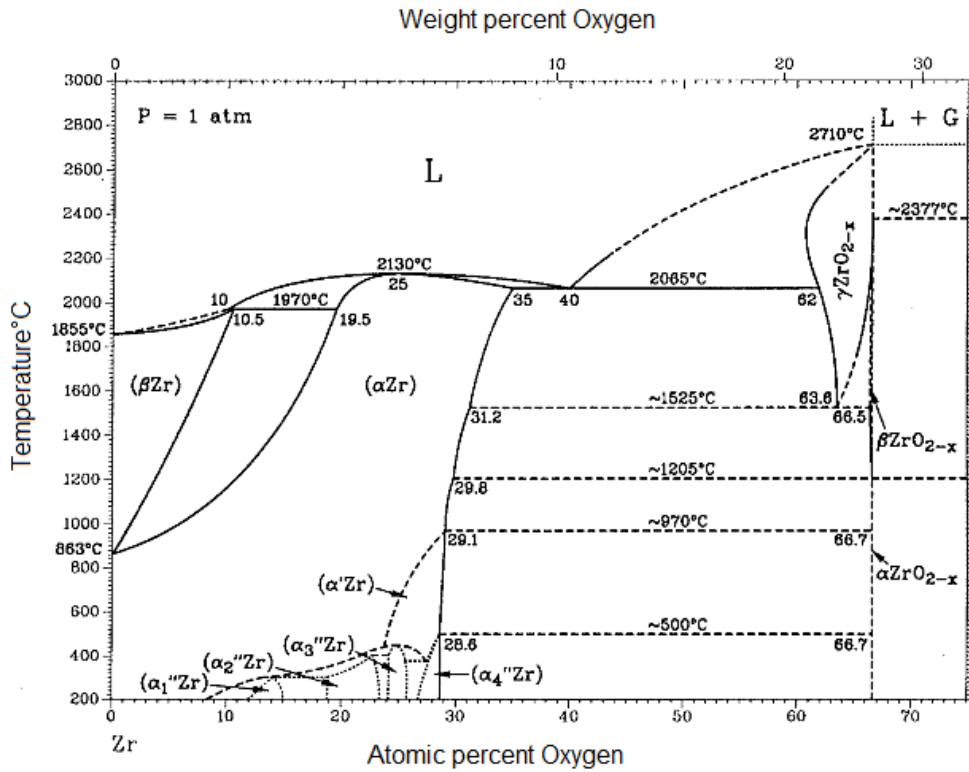
Figure 5: The zirconium –oxygen equilibrium phase diagram.[1]

Due to large affinity of oxygen for zirconium, a thin oxide is formed. The oxide layer has a high nucleation rate and the size of oxide grains is very small (typically less 5nm). The solubility of oxygen in a-zirconium is 28.6% at 500°C. At room temperature and low pressure (10^{-6} torr), three sub-oxides of Zr_2O, ZrO, Zr_2O_3 and ZrO_2 are reported to form initially on the surface, in both water vapour and oxygen atmosphere. It is thermodynamically favourable for the oxygen to be in solid solution in the matrix, but at room temperature the diffusivity of oxygen in zirconium is limited[1].

Chapter 3: Transformation behavour of zirconium and zirconium alloys

3.1 Introduction

The temperature range of transformation for pure zirconium is between 980°C and 865°C. Only the α phase is present below this temperature range. Massih agrees with Holt that the β to α phase transformation, on cooling, in Zircaloy alloys, can produce a basket-weave or a parallel-plate structure[5]. The basket-weave structures appear as relatively short intersected plates within the parent β-grains. A basket-weave structure results from random precipitation of alpha plates on a number of planes in one beta grain. In contrast, the parallel plate Widmanstätten structure results from the precipitation of alpha plates on the same habit plane in one prior beta grain. Refer to Figure 6 for images of parallel-plate and basket-weave structures.

Cotie states that the cause of the basket-weave structure is the abundant supply of nucleation sites for alpha within the beta grain[6]. From each site, the alpha plates could grow on the many habit planes provided by the cubic beta structure. These plates are quite short since they cannot grow very long before they meet other plates. The result is a basket-weave structure. In the absence of such nucleation sites, the alpha plates must nucleate on the grain boundaries, resulting in a parallel plate structure[6]. Cotie quotes Okvist and Kallstrom in stating that the alpha plates in the basket-weave structure nucleated on second phase particles of 0,4 µm diameter and consisted of a particle density of 5×10^5 per cm^3.[6] The particle size of second phase particles would then be expected to be a function of the composition of the base material and heat treatment of the material. The heat treatment would control the segregation of alloying elements (iron, chromium and nickel) that form second phase particles.
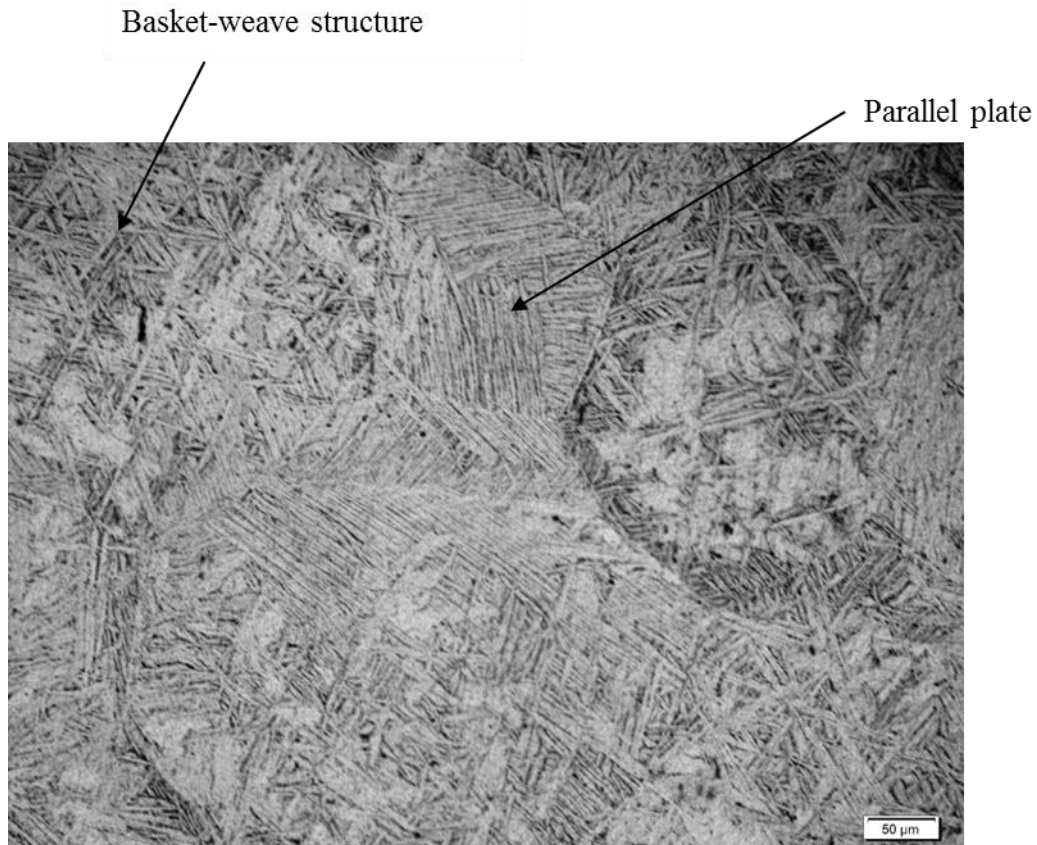
Figure 6: A mixture of basket-weave and parallel plate structures in a Zircaloy-2. Current study: autogenous gas tungsten arc weld metal performed at 35 A, 10V and 0.95mm/s [7]

3.2 The effect of cooling rate on transformation behaviour

Holt isothermally heat-treated Zircaloy-4 samples at temperatures of 1000°C to 1100°C at times intervals of two minutes to four hours. The samples were then cooled in air. Holt found that the transformation products of the β to α transformation, during cooling from a high temperature, were independent of the beta soaking temperature and independent of the beta grain size. Holt found that cooling rates from 2 to 200 °C/s produced fine Widmanstätten plates. Cooling at 2000 °C/s produced a quenched martensitic structure, as seen in Table 2[8]. Perez & Saggese also did a series of experiments in which the cooling rate was varied. The observed microstructures are noted in Table 2[9],[10].

Table 2: Summary of microstructures in Zircaloy-4, after cooling at different cooling rates (in ºC/s), as reported by two authors

Transformation product	Holt[8],[10]	Perez& Saggese[9]
Martensite	2000	≥1500
Mixed structure of martensite and basket-weave	not reported	1500-600
Basket-weave	200 - 20	600 - 10
Intermediate basket-weave and parallel plate	not reported	10 - 2
Parallel plate	not reported	2 - 0.5
Lenticular	not reported	≤0.5

Massih found that Zircaloy-2 and Zircaloy-4 billets, that contained 50–120 ppm carbon, 20–50 ppm silicon and 5–10 ppm phosphorous, formed a basket-weave structure after being water quenched from the β phase. Carbon, silicon, and phosphorus form inclusions in these zirconium alloys. Carbon, silicon and phosphorus have low solubility in zirconium and may act as nucleation sites for the basket-weave structure. Inclusion free zirconium materials form parallel-plate structures on prior beta grains[5].

From the information in Table 2, in Zircaloy-4, a high cooling rate (10 to about 600^0C/s) resulted in a basket-weave structure, while a lower cooling rate (below about 2^0C/s) resulted in a parallel plate structure. Similar data on Zircaloy-2 could not be found. Zircaloy-4 has a higher Fe (0.18-0.24%) content compared to Zircaloy-2 (0.07-0.20%) and no Ni as shown Table 1. The Fe content is considered not to be high enough to affect transformation from β to α. It is considered likely that, as in Zircaloy-4, a high cooling rate will favour basket-weave structure in Zircaloy-2, and a low cooling rate will result in a parallel plate structure. This is due to the formation of second phase particles (SPPs) which are possible nucleation sites for basket-weave structures[8].

3.3 Second phase particles in zirconium alloys

In zirconium alloys, iron, nickel and chromium in solid solution at high temperatures lead to the formation of intermetallic compounds which are mostly found on the grain boundaries and triple points along the boundaries[11],[12]. These compounds (Zr_3Fe, $NiZr_2$, and $ZrCr_2$) are brittle and can absorb large amounts of hydrogen[12]. The early stages of nucleation and growth of second phase particles (SPPs) occur by diffusional growth of isolated, non-interacting precipitates. Microclusters of atoms containing alloying elements like iron and chromium will form along the grain boundaries. It is generally assumed that, initially, the second phase particles have a uniform dimension. Coarsening occurs when the particle size distribution develops towards the end of the nucleation, as larger particles grow at the expense of smaller particles. Figure 7 shows SPPs in a chain like formation after being β quenched. [5]
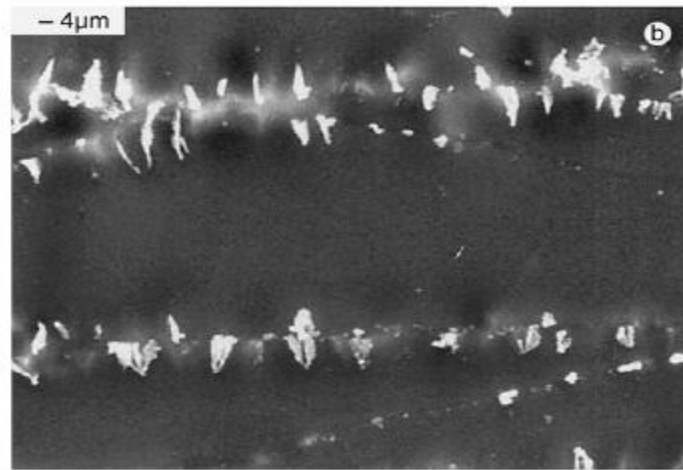
Figure 7:   Second phase precipitates in a chain like formation after β-quenching of Zircaloy-2 specimens from 1323K at 6.6°C/s[5]

Alloying elements can be divided into thermal fast diffusing elements and thermal slow diffusing elements. Thermally fast diffusing alloy elements such as chromium, iron and vanadium are associated with reversible phase transformations upon heating and cooling[13]. Thermally slow-diffusing elements such as nobium or molybdenum show metastable phase transformations and are characterised by a partial transformation of β and the precipitation of second phase particles on cooling.

Figure 8 depicts the heating and cooling peaks at a rate of 5°C/min on Zircaloy-4 alloy. The peak corresponding to the heating cycle is assumed to be endothermic and corresponds to the transformation of $Zr(Fe, Cr)_2$ to β-Zr, and the second peak corresponds to the transformation of α-Zr to β-Zr. On cooling, the exothermic peaks correspond to the inverse reactions.[13] It can be noted the formation of SPPs in Zircaloy-2 was reported at a cooling rate of about 6.6°C/s on Figure 7 and at 300°C/s on Figure 8.
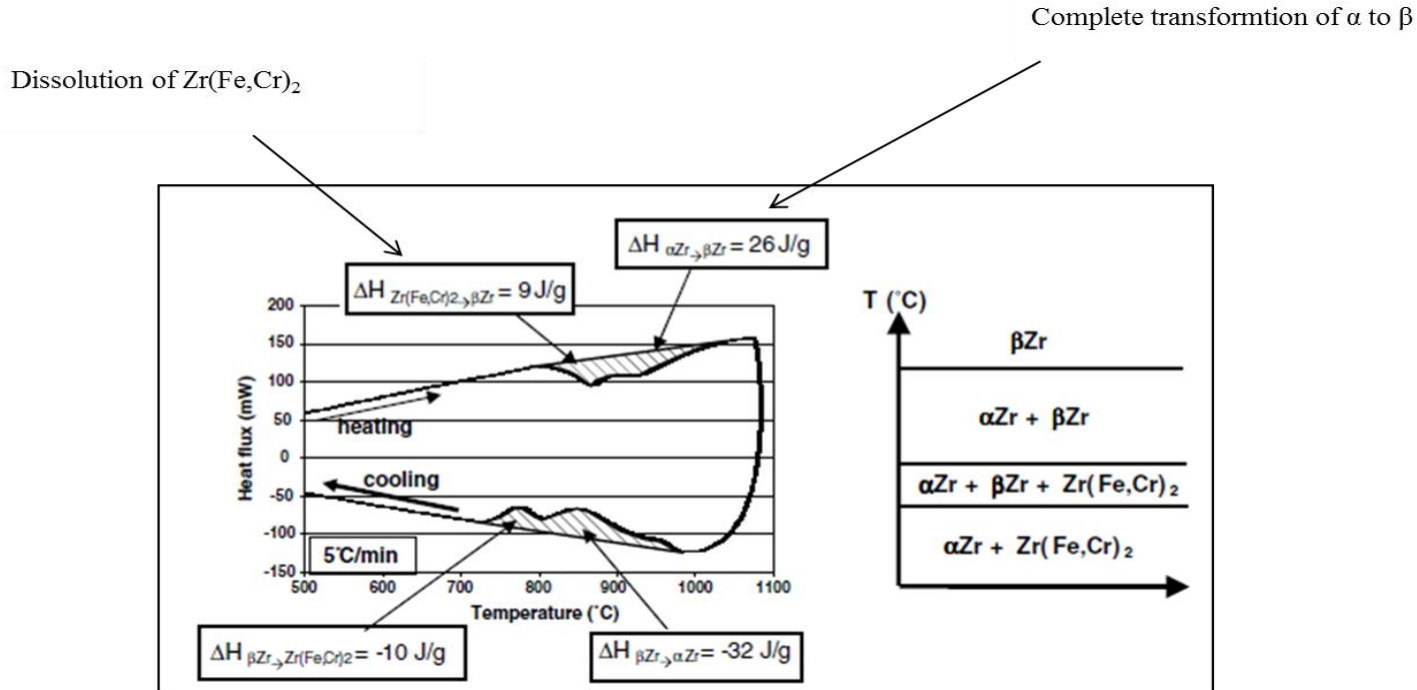
Figure 8: The formation and decomposition of SPP of Zircaloy-4 with composition of Zr– 1.2%Sn–0.2%Fe–0.1%Cr using a calorimetric technique at a heating and cooling rate of 5°C/min[13]

To conclude this section, it is evident that the transformation behaviour of zirconium is largely influenced by composition of the specific zirconium grade and cooling rate. It is possible to influence the cooling rate of the weld metal and the heat affected zone by changing the heat input during welding. High heat input welds result in lower cooling rates compared to low heat input weld. A change in heat input may therefore change the microstructure of the welded joint. Specifically, a higher heat input will result in lower cooling rates, and the formation of a parallel-plate structure rather than a basket-weave structure.

3.4 Dilatometry studies of zirconium

Saibaba performed dilatometry experiments on heat treated Zr 2.5% nobium alloy. Several quenching rates were investigated from 0.06 to 100°C/s[14].

Figure **9** shows the heating and cooling curves. On heating, the transformation beginning and transformation end temperatures were 694 to 716°C and 874 to 879°C. Lustman published results of thermal dilation curves done on Grade 1 WAPD crystal bar zirconium. On heating, the transformation start temperature was reported as 853°C and the transformation end temperature as 902°C [15].

The dilatometry curves showed a contraction as the transformation from alpha to beta occurs. Such contraction is apparently inconsistent with the fact that alpha has a hexagonal closely packed (hcp) structure, and beta a bcc structure. Skinner *et al*. attributed this contraction to the differences in thermal expansion of the two phases[16]. The thermal expansion of hexagonal zirconium between 298 K and 1143 K is $5.3 \times 10^{-6} K^{-1}$ along the *a* axis and $10.8 \times 10^{-6} K^{-1}$ along *c* axis. For a randomly oriented polycrystalline sample, the thermal expansion is $7.2 \times 10^{-6} K^{-1}$. The average value for the linear coefficient of cubic zirconium between 1143 K and 1600 K is $9.7 \times 10^{-6} K^{-1}$. At the transition between alpha and beta there is a decrease in volume of 0.66%. [16]
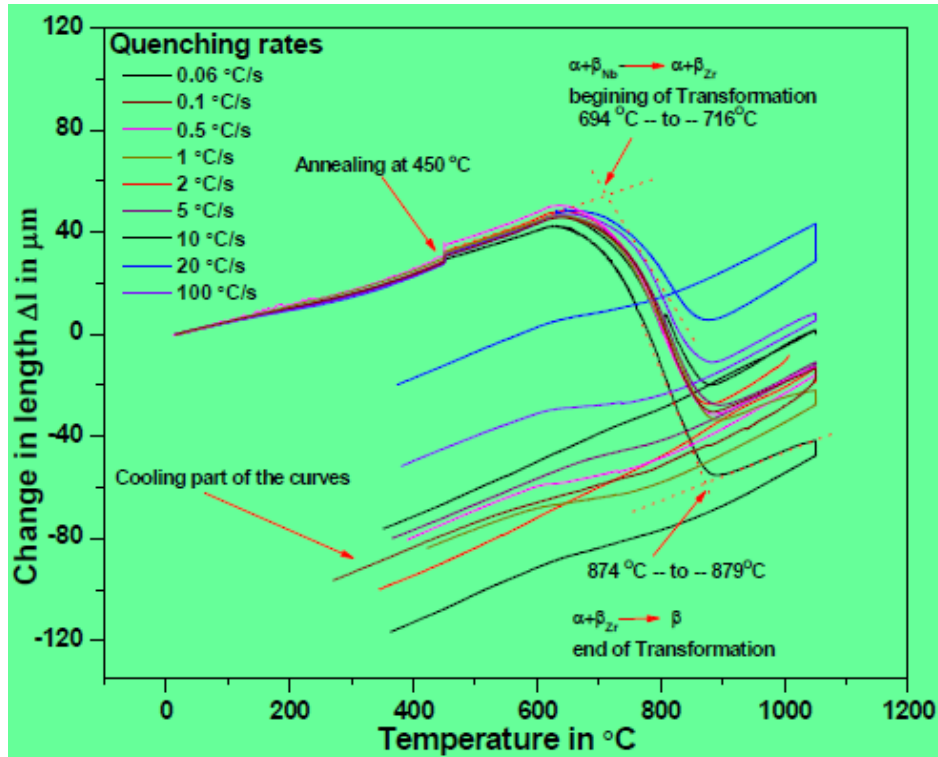
Figure 9 : Dilatometry curves of heat treated Zr-2.5 nobium alloy that was quenched from 0.06°C -100°C taken from Saibaba[14]

3.5 Irradiation effects on zirconium

Irradiation damage of zirconium alloys is mainly caused by fast neutrons. Fast neutron irradiation negatively influences the microstructure of the metal. Dislocation loops are formed and may develop into a network structure. The nucleation and growth of the loops are caused by the super-saturation of vacancies and interstitials induced by the irradiation. Two types of irradiation induced dislocations have been observed to exist, <a> and <c>-type. The dominant type of dislocation is the <a> type and is associated with high irradiation.

The formation of a <c> type of dislocation is associated with the start of steady state irradiation growth in recrystallized material. Irradiation causes the metal to expand and the cladding tube to lengthen[6].

27

3.6 Effect of irradiation on second phase particles

Irradiation causes morphological and structural changes of the second phase particles in Zircaloy grades. Griffiths et al studied the morphological changes of $Zr_2(Ni, Fe)$ and $Zr(Cr, Fe)_2$ intermetallic particles due to irradiation as a function of temperature. Griffiths et al found that 77°C, $Zr_2(Ni, Fe)$ and $Zr(Cr, Fe)_2$ both become amorphous, between 247-327°C $Zr_2(Ni, Fe)$ remain crystalline while $Zr(Cr, Fe)_2$ becomes amorphous and that between 367-437°C both experience radiation-induced dissolution. At the higher temperatures, a redistribution of alloying element results in the formation of precipitates in the matrix and at the grain boundaries. Sn-rich precipitates are also formed at these temperatures, due to radiation-enhanced diffusion[6].

Chapter 4: Practical guidelines for the welding of zirconium alloys

4.1 Contamination and gas shielding

Ettienne noted that zirconium is very sensitive to hydrogen, oxygen and nitrogen. Zirconium welds become brittle when exposed to these elements[2]. Thus, proper shielding when welding zirconium is extremely important. Furthermore, the shielding has to be done on both sides of the material. A trailing gas is used to shield the top of the weld while a backing plate is used to shield the bottom of the weld. It was suggested that the shielding is not to be removed until the temperature of the work piece is below 480°C. Figure 10 shows an image of a trailing shield attached to a torch for gas tungsten arc welding[18].
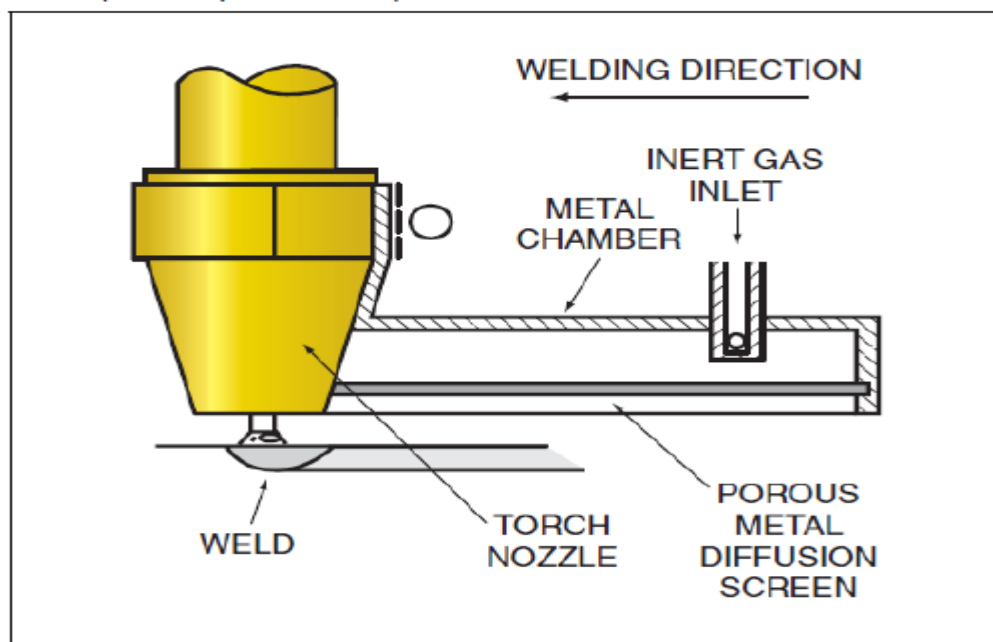
Figure 10:Trailing shield attached to torch for gas shield arc welding of titanium and other reactive metals[18]

A glove box may also be used to create an inert environment while welding. However, the use of a glove box limits accessibility of the work piece by the operator. Also, to create an inert environment inside a glove box is time-consuming. These glove boxes can also be used in vacuum.[2]

There is a spectrum of colours which indicate the level of oxidation by a weld, as noted by Ettienne:

silver – light yellow – dark yellow – light blue – dark blue – light gray – dark gray[2]

According to SANS 15614-6, for titanium and zirconium, the acceptable colour of the weld metal surface is silver or straw. Darker brown, purple, blue, grey and flaky white surfaces are not acceptable[17]. The SANS 15614-6 requirement is therefore consistent with the change in colour with an increasing degree of oxidation, as noted by Ettienne.

4.2 Preheat and post weld heat treatment

Generally, no preheat or post weld heat treatment is required except if it is deemed necessary to reduce the residual stress in welded joints in commercial grade zirconium[2].

4.3 Hardness testing of welds

Hardness measurements are recommended as a check for adequate gas shielding. An average value of 200 HV is reported for grade 702, an unalloyed commercial grade of zirconium[2]. No published hardness values for contaminated welds could be found.

Chapter 5: Experimental procedure

5.1. Base metal

Nuclear grade zirconium 1.5%Sn with a thickness of 1.2 mm was used for this investigation. The material was selected based on availability. Table 3 gives the chemical composition of the base metal and that of Zircaloy-2 and Zircaloy-4. The chemical composition of the base material used in this investigation did not strictly adhere to specification limits Zircaloy-2. Specifically, the absence of nickel would indicate that the base metal was zirconium 1.5%Sn. The iron content met the Zircaloy-2, but not the Zircaloy-4 requirements. This suggests that the base metal is a zirconium 1.5%Sn that is off specification.

Table 3: Chemical composition of the base metal used in this study (single figures are maximum values.)

Element	Sn	Cr	Fe	Ni	O	Nb	Hf
Specification limit Zircaloy-2[3,4] -	1.2-1.7%	0.05-0.15%	0.07-0.20%	0.03-0.08 %	1400 ppm	-	100 ppm
Specification limit Zircaloy-4-[3,4]	1.2-1.7%	0.07-0.13%	0.13-0.24%	-	1400 ppm	-	100 ppm
Actual composition	1.5%	0.09%	0.087%	No Ni detected	No O detected	< 58 ppm	50 ppm

5.2. Gas tungsten arc welding

This investigation used the gas tungsten arc welding (GTAW) process, as this process is commonly used to weld nuclear grade zirconium[2]. Mechanised gas tungsten arc welding was performed using a Lincoln Electric Square Wave TIG-355 welding machine fitted with high frequency arc starting. The welding torch was stationary. The samples were clamped to a backing plate and translated at various speeds ranging from 0.95 to 4.08 mm/s. The welding current was set on the welding machine to the nearest ampere.

A two-step arc start method was used for arc initiation. This method involved pressing and holding the foot pedal for the arc to initiate and releasing the pedal to terminate the weld. The welding voltage was manually observed on the built-in voltmeter during welding, to the nearest volt. Figure 11 shows the experimental setup.
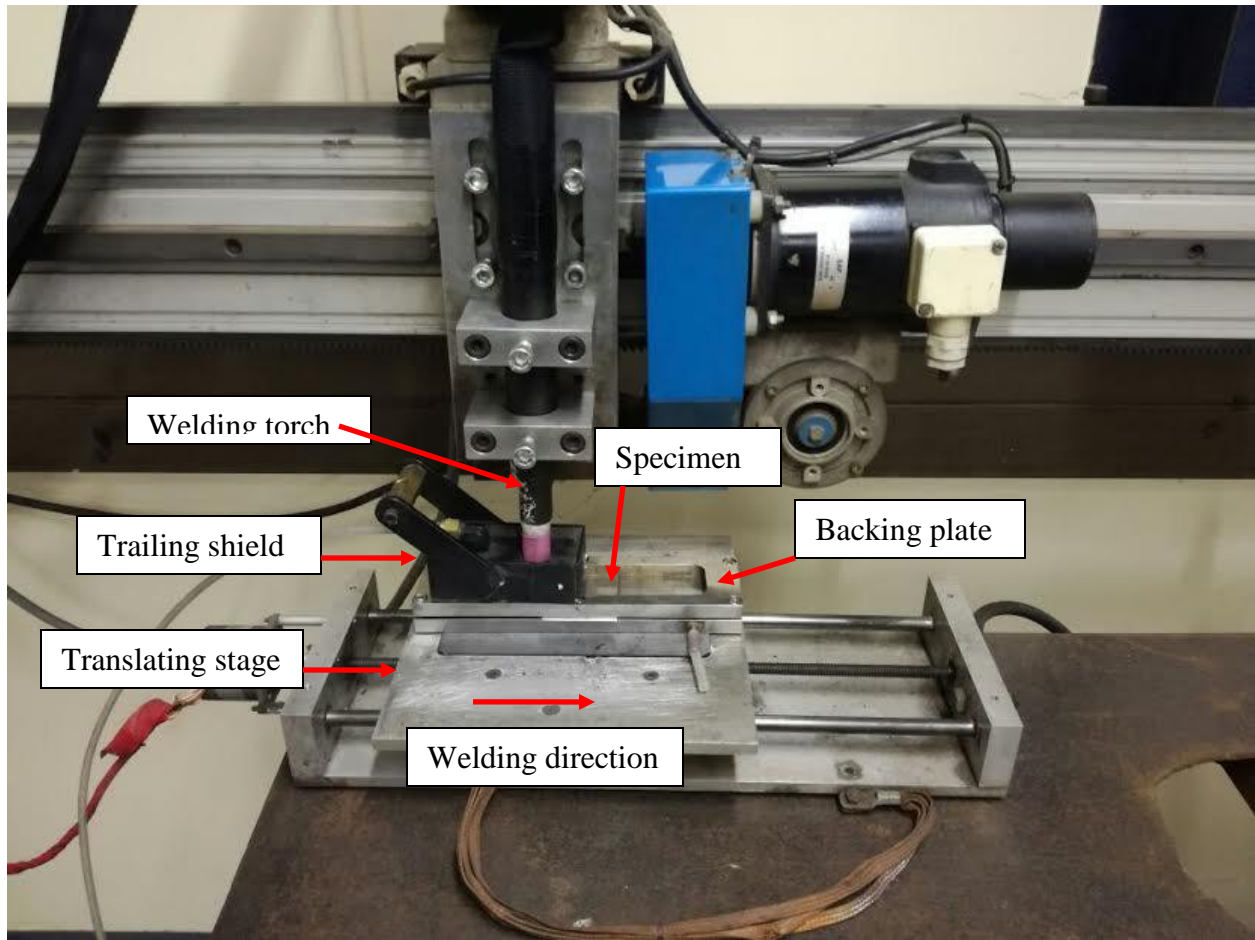
Figure 11: Experimental setup for mechanised welds

Autogenous bead-on-plate welds with back purging were done. Technical grade argon (99.9% purity) was used as welding gas, back purging and for the trailing gas shield. A range of trailing gas shielding flow rates was tested and the optimum was used as listed in

Table **4**. The pre-flow and after flow of the welding gas were 3 seconds and 15 seconds, respectively. A tungsten electrode with 2 % ThO_2 addition was used with DCEN polarity. The

diameter of the electrode was 2.4 mm and the electrode tip angle was machined to a constant angle of 60°. A constant arc length of 2 mm was used on all welds.

Table **4** lists welding variables for the bead on plate welds, based on the list of welding parameters as noted in ASME IX for gas tungsten arc welding.[18]

Table 4: Welding variables for the different weld beads; the classification of variables as defined in ASME IX for gas tungsten arc welding

Paragraph as per ASME IX	Variable	Value
QW-402.1	Groove design	Bead-on-plate
QW-402.5	Backing	None
QW-402.10	Root spacing	Not applicable
QW-402.11	Retainers	Mechanical clamps
QW-403.6	Thickness	1.2 mm
QW-404.3	Filler metal	Not used
QW-405 .1	Position	Flat
QW-406.1	Preheat temperature	Ambient
QW-407.1	Post-weld heat treatment	Not used
QW-408.1	Shielding gas	Technical grade argon
QW-408.3	Flow rate	15 liters per minute
QW-408.5	Backing gas flow rate	15 liters per minute (includes gas flow to trailing gas shield)
QW-408.9	Backing gas	Technical grade argon
QW-408.10	Trailing gas	Technical grade argon
QW-409.1	Heat input	Refer to Figure 12
QW-409.3	Pulsing current	Appendix A
QW-409.4	Polarity	DC electrode negative
QW-409.8	Welding current and voltage	Appendix A
QW-409.12	Tungsten electrode	EWTh-2 2.4 mm diameter
QW-409.13	Tip angle	60°
QW-410.1	String /weave	String
QW-410.3	Orifice, cup, or nozzle size	16 mm bore (no.10, 5/8 in.)
QW-410.5	Method of cleaning	Acetone
QW-410.6	Method of back gouge	None
QW-410.7	Oscillation	Not used
QW-410.9	Multi to single pass/side	Single pass from one side
QW-410.11	Closed to out chamber	Out-of-chamber
QW-410.25	Manual or automatic	Mechanised

5.3 Matrix of welding parameters

A matrix of pulsed and non-pulsed welds, with welding current and welding speed as the main variables, were used, as seen in

Figure **12**. The matrix was designed to test the limits of the welding process and welding mode for the base metal thickness as well as the region where suitable welds can be made. A total of 19 welds of both pulsed and non-pulsed were done. The pulse parameters were: 70% of the pulsed period at full current and 30% of pulse period at a low current of 20% of the peak current. This procedure was done to investigate the effect of pulsing on the structure and properties of the weld metal. The pulse frequency was 3 pulses per second. Of the nineteen welds, one combination of welding current and welding speed resulted in burn through. Another combination of current and speed did not result in fusion; refer to section 6.4.2 for details contaminated welds that were made using improper shielding.
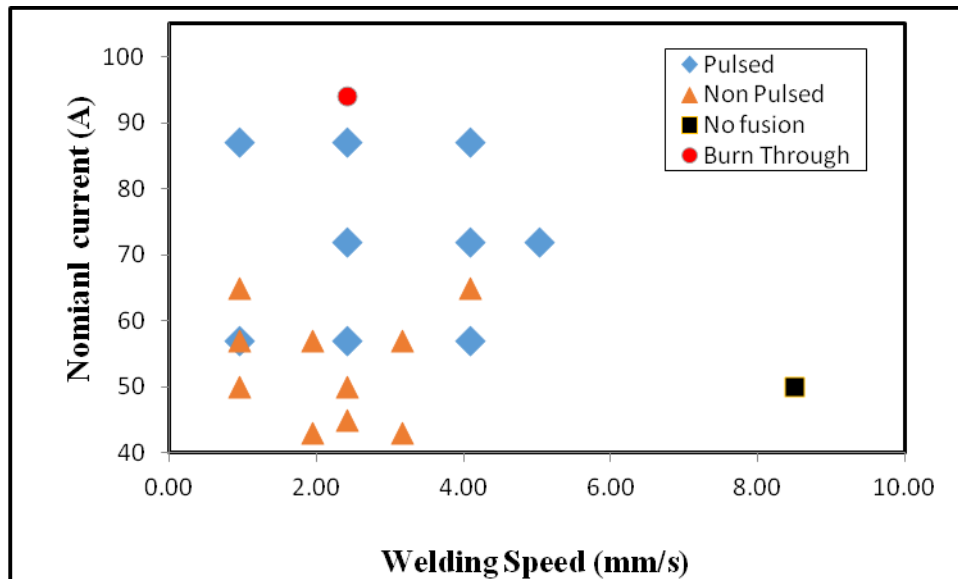
Figure 12: Experimental matrix of welding current and welding speed, for pulsed and non pulsed welds.

5.4. Dilatometry

The dilatometry samples were cut from the same base material used for welding and folded double to increase the stiffness and avoid mechanical deformation when clamped in the dilatometer. Folding the specimen sometimes results in the formation of a crack on the tensile

surface. A dilatometry sample can be seen in Figure 13. The experiments were done on a Dil 805 Bähr dilatometer. A new sample was used for every dilatometry run. Dilatometry involved two heat treatment cycles. The objective of the first heat treatment cycle was to anneal the cold work associated with the folding of the plate samples. The annealing cycle was done by heating the samples to 1100°C at a heating rate of 5°C/s, followed by a soaking period of 5 minutes and cooling at a rate of 5°C/s to 200°C. The annealing was designed to give the dilatometry sample enough time at elevated temperatures to relieve residual stress caused by the mechanical deformation of folding. Given the peak temperature, the α − β phase transformation occurred during the annealing cycle.

The second heat treatment cycle simulated the weld thermal cycle in the high temperature heat affected zone by heating from 200 to 1100°C at 100°C/s, a brief soaking period (10s) and cooling at a specific cooling rate. The peak temperature during dilatometry was a compromise between simulating phase transformations in the high temperature heat affected zone (indicating the use of a high peak temperature) and reliability of the intrinsic thermocouple (that indicated a lower peak temperature). Six different cooling rates were used: 600, 300, 110, 50, 11 and 1.1°C/s. Figure 14 and Figure 15 show the heat treatment cycles for 1100 and 900°C peak temperatures.

These cooling rates approximately covered the range of cooling rates previously published for Zircaloy-4, that is 0.5 to 2000°C/s – Table 2. Three dilatometry samples were heated to a peak temperature of 900°C on the second heat treatment cycle, these samples were cooled at 0.9, 9 and 90°C/s respectively. This procedure was done to investigate the alpha to beta transformation at a peak temperature of 900°C.

The dilatometry heat treatment cycles were done in a helium environment. After the heat treatment in the dilatometer, the sample had a darker surface, indicating some contamination by gaseous elements.

Figure 13: Dilatometry samples; left hand side sample side shows a dilatometry that has not been heat treated and the right hand side sample shows a heat treated sample.
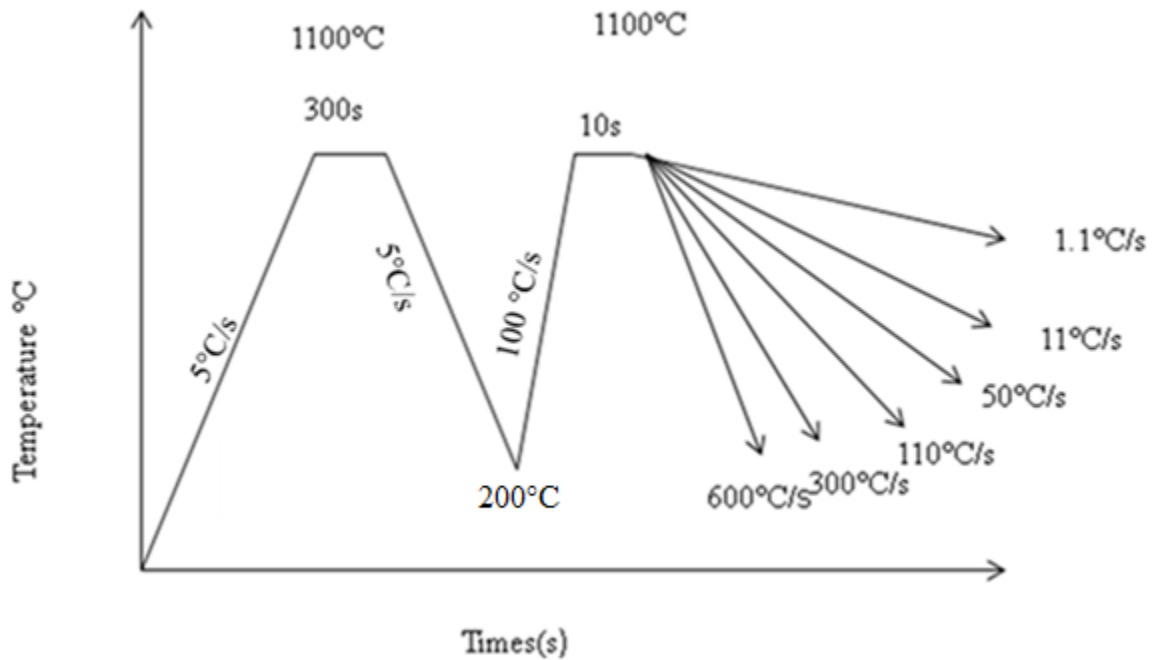
Figure 14: Schematic showing heat treatment cycle for 1100 °C peak transformation temperature of dilatometry samples.
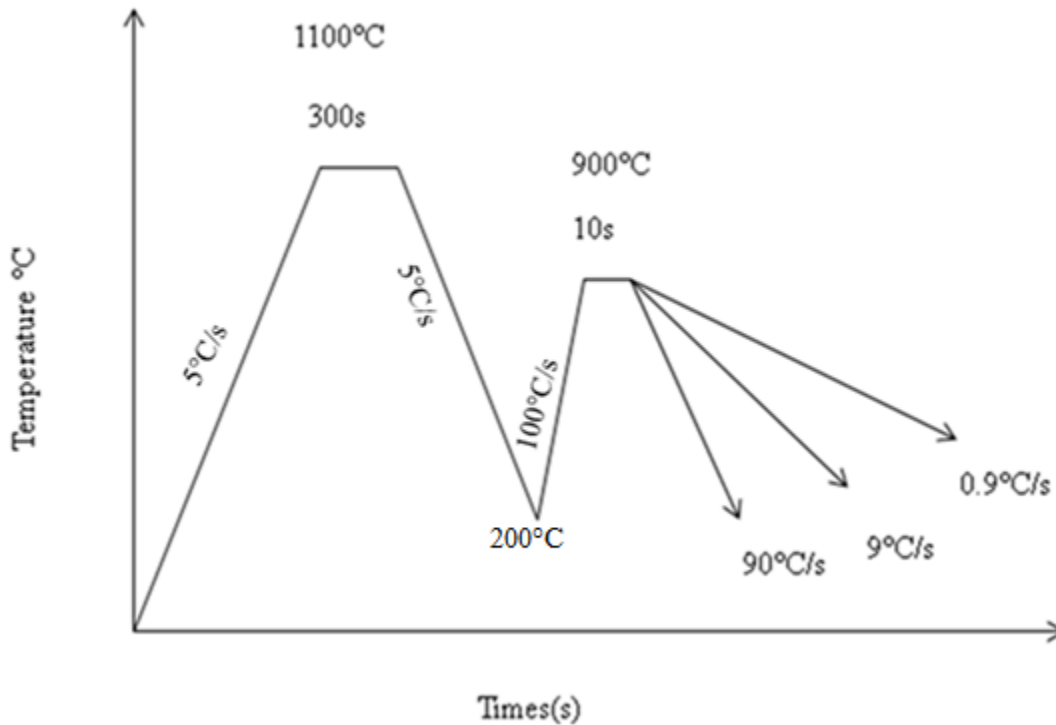
Figure 15: Schematic showing heat treatment cycle for 900°C peak transformation temperature dilatometry samples.

5.5. Metallographic techniques

In this study, the orientation of the polished section for the weld was the top view, that is, the polished surface was parallel to the original sheet surface. This orientation was chosen to sample as large a weld metal surface as possible. One sample was polished in cross section view for comparison purposes. For dilatometry sample, the longitudinal surface, as shown on Figure 16**,** was ground and polished. Mounting and polishing techniques are not discussed in cited literature. In the current study, metallographic preparation involved grinding at 80, 400, 600, 800 followed by 1200, 4000 grit paper. The final polish was done with colloidal silica.
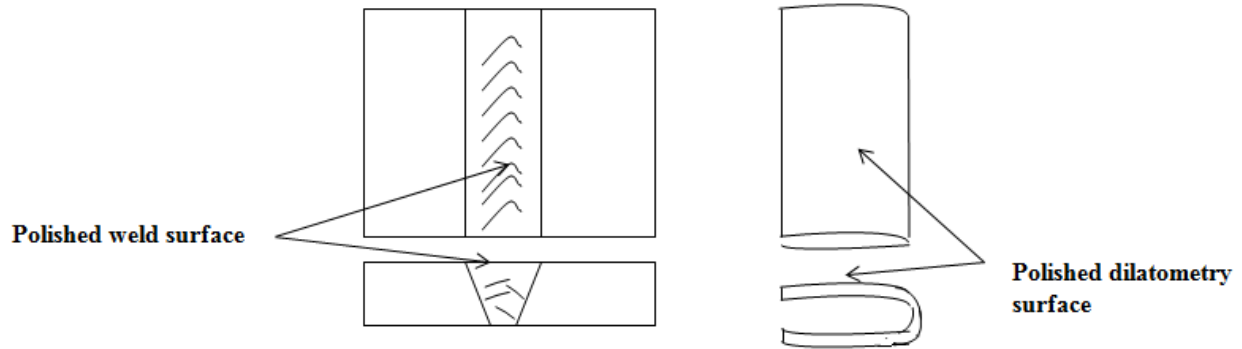
Figure 16: Orientation of polished surfaces for welds and dilatometry

Electrolytic polishing is rarely performed on zirconium and only a few authors are cited as having used this technique. Bangaru used a 10% perchloric acid and 90% ethanol mixture or a 5% perchloric acid and 95% acetic acid mixture on Zircaloy-4[19]. The polishing voltages quoted were 70V and 40V, respectively, and the polishing temperatures were 50 and 13°C, respectively.

Various etchants are used for the etching of zirconium. Most of the etchants cited in literature contain H_2O, H_2O_2, HNO_3 or HF. Vandervoort discussed the roles of each of the reagents in the chemical solution. HF attacks the surface the material while HNO_3 prevents staining[20]. Water, or hydrogen peroxide, acts a solvent. As the solution is very acidic, the samples should be swabbed. Shabaan *et al* etched Zircaloy-2 with a solution of 10 % HF, 45 % HNO_3 and 45 % H_2O[21]. Ahmad etched Zircaloy-2 with a solution of 50% H_2O_2, 47% HNO_3 and 3% HF[22]. Baek & Jeong prepared samples by chemical etching Zircaloy-2 with a solution of 10 % HF, 45 % HNO_3 and 45 % H_2O.[23] Ahmad revealed the microstructure of Zircaloy-2 by chemical etching with a solution of 50 ml H_2O_2, 47 ml HNO_3 and 3 ml HF and with H_2O_2: 45 ml, HNO_3: 45 ml and HF: 10 ml respectively.[24],[25]

Table 5 summarizes the different etching reagents discussed. The etchant used during this study contained 3 % HF, 47 %, HNO_3 and 50 % H_2O_2. This specific etchant composition was chosen because the ratio of nitric acid to hydrofluoric acid should be a minimum of 10:1 to prevent hydrogen pickup during etching[20]. The etchant used by reference 16 was used in the current study, as noted in Table 5.

Table 5: Summary of relevant etchants used in previous metallographic studies.

Reference No	Year	HF	HNO₃	H₂O	H₂O₂
13	1977	10	45	45	No present
14	2001	3	47	not present	50
15	2002	10	45	not present	45
16	2005	3	47	not present	50
17	2006	10	45	45	not present
Published range of concentration		3-10%	45-47%	0 or 45-50%	0 or 45-50%
current study		3	47%	not used	50

5.6. Hardness

Vickers hardness tests were done on the welded samples and dilatometry using a load of 2900 mN (0.3 kg) and a dwell time of 10s. A mechanised hardness machine at the CSIR and a manual Vickers hardness at University of Pretoria were used to perform the hardness measurements. The indents were spaced 0.5 mm apart and the indentations were made starting from one edge of the HAZ through the weld and ending on the edge of the HAZ at the opposite side. The indentations on the dilatometry samples were made randomly. Similarly to the hardness indentations on the welded joint, the spacing of the indentations on the dilatometry samples was at least 0.5 mm.

5.7. Quantitative metallography

The procedure to measure the fraction basket-weave structure started with the construction of a grid consisting of 100 points in the form of 10 x 10 matrix on a transparent sheet. This grid was randomly superimposed on an image of the optical microstructure. A point on the grid was marked according to the microstructure type the point fell on (basket-weave/ parallel-plate structure). The sum of all the points on the grid was calculated and expressed as a percentage of basket-weave structure for the weld and HAZ. The grid always covered more that 60% of the weld metal. A 95% confidence interval was calculated from the standard deviation using the Underwood equations[26](see Equations 1and Equations 2). The magnification was set at 20x . More than one structural feature was avoided in selecting a magnification.

$$\left(\frac{\sigma(P_p)^2}{P_p{}^2}\right) = \frac{1}{P_\alpha} \quad \text{Equation 1}$$

95% confidence interval=1.96* $\sigma(P_p)$ Equation 2

The linear intercept method was used to estimate the β grain size. A grid consisting of cells that are 10 x10 mm of known length was drawn on the microstructure. The number of times the line intercepted the grain boundary was counted. The length of the line running through the grain boundaries was then divided by the number of intercepts and an average grain intercept length was calculated. A standard deviation of the measurements and a 95% confidence interval were calculated. The magnification on the optical microscope was calibrated to ensure accuracy of measurement

Chapter 6: Results

6.1 Welding parameters

Welding current, voltage, speed and average weld width were measured. For this study, it was assumed that the arc voltage was identical to the welding voltage. From the weld width, the heat input was calculated using the thin-plate Rosenthal equations. Thereafter, the heat input was used to calculate the arc efficiency; the calculated arc efficiency was compared to published values. From the heat input, the cooling time from $900^{o}C$ to $600^{o}C$, (Δt_{9-6}.) was calculated. A summary of the welding parameters can be seen in Appendix A.

6.2 Arc efficiency and cooling time from 900 to 600°C(Δt_{9-6})

Rosenthal equations were used to calculate the arc efficiency. The conditions for which the Rosenthal equation is valid are the following.[**Error! Bookmark not defined.**]

- The plate is semi-infinite.

- A moving point source (or line) represents the welding arc. This assumption leads to a prediction of an infinite temperature under the arc, therefore, the solution is a reasonable approximation only some distance away from the heat source. Rosenthal indicated that it should only be used at, and beyond, the fusion boundary (in the HAZ).

- Material properties such as thermal conductivity and specific heat are unaffected by changes in temperature or state (solid or liquid).

- Heat transfer is by conduction only (no heat loss due to radiation or convective flow). Heat losses at the plate surface are negligible.

- Latent heat changes due to phase transformations are neglected.

The thin-plate Rosenthal equation was used to estimate the weld thermal cycle in the heat affected zone.

The following thermal properties were used at an absolute temperature of approximately $T_m/3$. The melting point T_m was taken as 2125K (1852°C)[27]

- thermal diffusivity $a = 7.8 \times 10^{-6}$ m².s⁻¹, [28]
- thermal conductivity $\lambda = 16$ J.m⁻¹s⁻¹.K⁻¹, [28]

From these values, the volume thermal capacity was derived as:

$\rho = \lambda/a = 2.05 \times 10^6$ J.m⁻³.K⁻¹ ·

Equation 3 was used to calculate the heat input from the width of the weld bead (see **Error! Reference source not found.**). This heat input was used throughout this document. Equation 4 was used to calculate the cooling time 900 to 600°C (Δt_{9-6}).

Equation 3 is presented below and Figure 17 shows a schematic of average weld width measurement. This measurement was used to determine the distance (r) from the heat source

$$T_p - T_0 = \frac{(q/v)^`}{(d\rho 2r)} \sqrt{\frac{2}{\Pi e}} \qquad \text{Equation 3}$$

Equation 4 is used to estimate the time taken to cool between 900 to 600°C

$$\Delta t_{9-6} = \frac{(q/v)^{`2}}{4\pi\lambda\rho\theta_{\frac{2}{2}}^2 d^2} \qquad \text{Equation 4}$$

where

$$\frac{1}{\theta_{\frac{2}{2}}^2} = \frac{1}{(873-T_0)^2} - \frac{1}{(1173-T_0)^2} \qquad \text{Equation 5}$$

With:

T_p Peak temperature (°C or K)

T_0 preheating temperature (assumed to be 20°C, 293 K)

42

(q/v)   heat input (J/mm)

d   plate thickness (m)

r   distance from heat source (m)

ρ volume thermal capacity $(J.m^{-3}.K^{-1})$

a   thermal diffusivity $(m^2.s^{-1})$

λ thermal conductivity $(J.m^{-1}s^{-1}.K^{-1})$

Δt_{9-6} cooling time from 900 to 600°C (s)
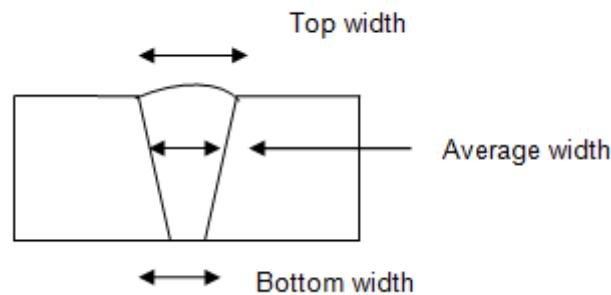
Figure 17: Schematic of average weld width measurement.

6.2.1 Current adjustment for pulsed welds

As stated in section 5.3, the pulsed welds were pulsed at 70 % peak current and the background was 20 % peak current. Thus the current was adjusted as follows

Adjusted pulse current = 0.7(Peak current) + (0.3)(0.2)(Peak current)
Adjusted pulse current = 0.76 (Peak current)

This adjusted pulsed current wasused in the calculation of the electrical heat input for the determination of the arc efficiency.

6.2.2 Calculations of arc efficiency

Error! Reference source not found. contains a summary of the average of weld width of zirconium alloy and the calculated heat input. The calculation for weld 7 was manually verified

to confirm the values in **Error! Reference source not found.**. As stated above, Rosenthal equations were used to estimate the weld thermal cycle in the heat affected zone.

The calculated Rosenthal heat input for weld 7 was determined using Equation 3 as follows:

$$T_p - T_0 = \frac{(q/v)^`}{(d\rho 2r)} \sqrt{\frac{2}{\Pi e}} \qquad \text{Equation 3}$$

$$q/_v = (d\rho 2r)(T - T_0)\sqrt{\frac{\Pi e}{2}}$$

$$q/_v = (0.0012)(2.05\text{x}10^6)(0.00213)(2)(2125 - 298)\sqrt{\frac{\Pi e}{2}}$$

$$q/_v = 40 \text{ J/mm}$$

The value for the heat input was therefore derived from the measurement of the average width of the weld bead, and not from the welding voltage, welding current and welding speed. The arc efficiency was calculated as a check on the estimated heat input. The electrical heat input of weld 7 was calculated using equation 7:

$$\left(\frac{q}{v}\right)_e = \frac{VI}{v} \qquad \text{Equation 6}$$

$$\left(\frac{q}{v}\right)_e = \frac{(9 \text{ V})(57 \text{ A})}{3.16 \text{ mm/s}}$$

$$\left(\frac{q}{v}\right)_e = 162 \text{ J/mm}$$

$$Arc \ efficiency = \frac{\left(\frac{q}{v}\right) \ (\text{from width of weld})}{\left(\frac{q}{v}\right)_e \ (\text{from elctrical heat input})}$$

$$Arc \ efficiency = \frac{40}{162}$$

$$\text{Arc efficiency} = 0.25$$

The arc efficiency varied between 0.11 and 0.44 (see Appendix A) with the average and median being 0.22 and 0.19, respectively, as seen in Figure 18. Moreover, the arc efficiency was similar to published values of 0.22 to 0.80[27]. There was no correlation of calculated arc efficiency with heat input, as seen on Figure 19.
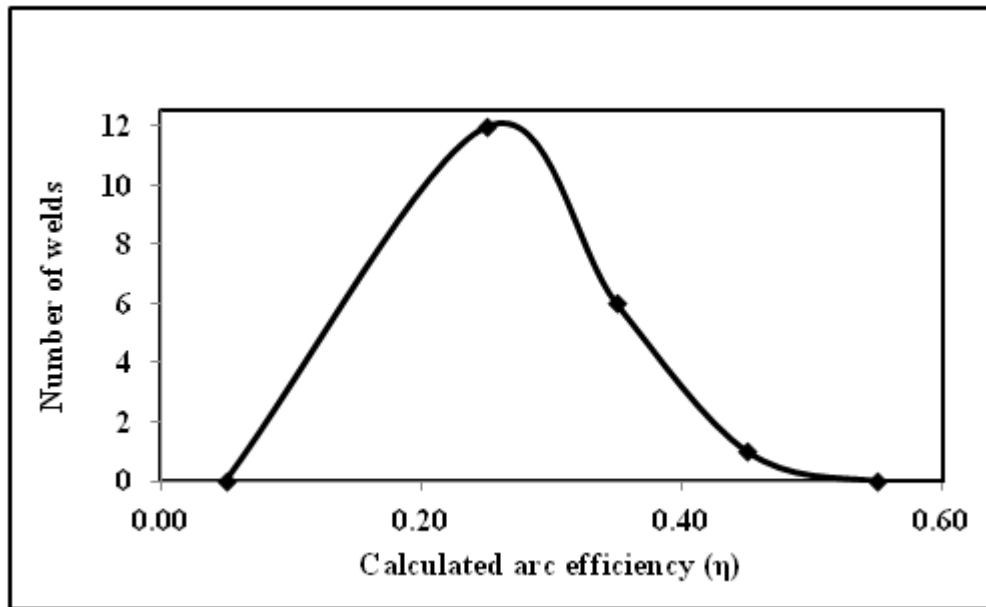
Figure 18: Distribution of calculated arc efficiency of the welds with median and average at 0.19 and 0.22, respectively.
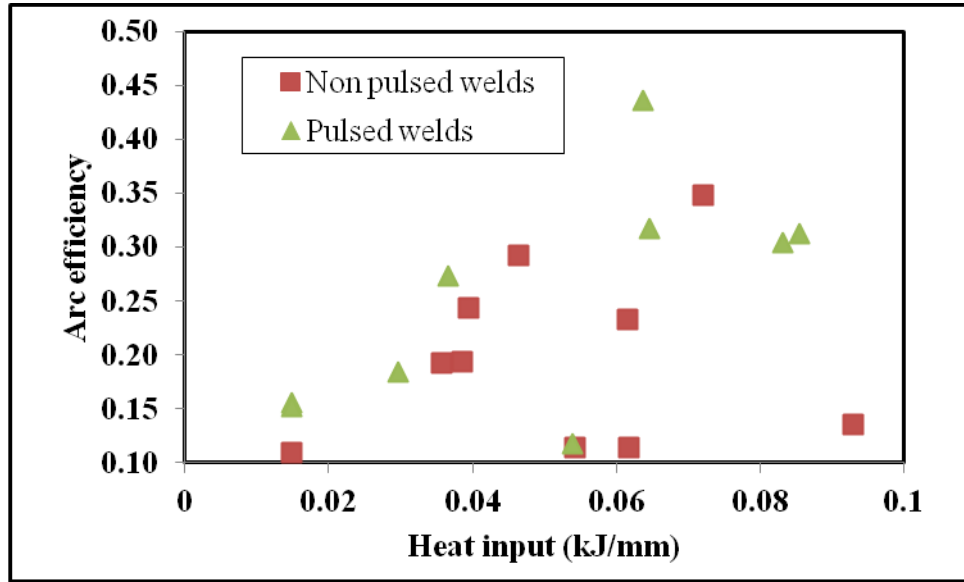
Figure 19: The variation of arc efficiency with heat input for both pulsed and non-pulsed welds. No correlation is observed .

6.2.3 Calculation of cooling time from 900 to 600°C (Δt_{9-6})

The Δt_{9-6} is the time taken for the weld to cool from 900 to 600°C. Δt_{9-6} is an important parameter in understanding the phase transformation behaviour from beta to alpha on cooling, as well as the resulting mechanical and metallurgical behaviour of Zircaloy-2 for both welds and dilatometry. Equation 2 was used to calculate Δt_{9-6}. Below, a sample calculation of Δt_{9-6} for weld 7:

$$\Delta t_{9-6} = \frac{(q/v)^{\cdot 2}}{4\pi\lambda\rho\theta_2^2 d^2} \qquad \text{Equation 7}$$

where $\frac{1}{\theta_2^2}$ is given

$$\frac{1}{\theta_2^2} = \frac{1}{(873-T_0)^2} - \frac{1}{(1173-T_0)^2} \qquad \text{Equation 8}$$

46

$$\frac{1}{\theta_2^2} = \frac{1}{(873 - 293)^2} - \frac{1}{(1173 - 293)^2}$$

$$\frac{1}{\theta_2^2} = 1.68e^{-6}$$

$$\Delta t_{9-6} = \frac{(0.04)^2}{4\pi 16(2.05e^6)(5.95e^5)(0.0012)^2}$$

$$\Delta t_{9-6} = 4.4s$$

6.2.4 Calculation of cooling rate 900°C to 600°C

The cooling time from 900 to 600°C was estimated as follows:

$$\text{cooling rate} = \frac{(900 - 600)°C}{4.41s}$$

$$\text{cooling rate} = 68°C/s$$

6.2.5 Sensitivity of arc efficiency to errors in the measurement of the welding voltage

The voltage was manually recorded during the welding cycle. The power supply recorded the welding voltage to the nearest volt. As a result, a recorded welding voltage of, for example, 9 volt, may have been, in the extreme, 8 volt or 10 volt. The effect of possible errors in the welding voltage, on the arc efficiency is considered in this section.

Table **6** shows the sensitivity of the calculated arc efficiency to an error in reading of the voltage at high and low heat inputs. An error in the welding voltage of one volt resulted in a small change in the calculated arc efficiency. Furthermore, the heat input used to calculate the cooling rate from 900°C to 600°C was based on the width of the weld bead (and not on the welding

voltage). The estimated cooling rate was therefore not sensitive to errors in the measurement of the arc voltage.

Table 6: Sensitivity of calculated arc efficiency to errors in welding voltage.

Weld No 7	Welding Voltage (V)	Welding current (A)	Welding speed (mm/s)	Bead width (mm)	Calculated arc efficiency
Actual voltage	9	57	3.14	4.25	0.24
Low voltage reading	8	57	3.14	4.25	0.28
High voltage reading error	10	57	3.14	4.25	0.22

6.3. Summary of heat input calculation, weld width, arc efficiency, quantitative metallography and hardness of the welds

Table 7 gives a summary of the weld width and average of weld width, as well as, calculated heat input and arc efficiency.

Weld 7 basket-weave structure 95% confidence calculation:

The variance is given by,

$$\left(\frac{\sigma(P_p)^2}{P_p^2}\right) = \frac{1}{P_\alpha} \text{ Equation 1}$$

Therefore,

$$\sigma(P_p) = \frac{P_p}{\sqrt{P_\alpha}}$$

Where:

$\sigma 2$ is the variance

$P\alpha$ is the number of points counted in the basket-weave microstructure

P_p point fraction in the basket-weave microstructure

$$\sigma(P_p) = \frac{0.9}{\sqrt{90}}$$

$$\sigma(P_p) = 0.0942$$

The 95% confidence interval is given by,

$$95\% \text{ confidence interval} = 1.96 * \sigma(P_p) \text{ Equation 2}$$

$$95\% \text{ confidence interval} = 1.96 * 0.0942$$

$$95\% \text{ confidence interval} = 0.19$$

Weld 7 grain size calculation:

The average of the grain size was determined as follows.

$$average = \frac{2x(200) + 67 + 9x(100) + 170 + 140 + 190}{15}$$

$$\text{Average} = 125\mu m$$

The standard deviation was calculated as follows.

$$\text{Standard deviation} = \sqrt{\frac{\Sigma(x_i - x_{avg})^2}{(n-1)}}$$

$$\sqrt{\frac{(190-125)^2 + (140-125)^2 + 2x(200-125)^2 + (70-125)^2 + 9x(100-125)^2 + (173-125)^2}{14}}$$

$$\text{standard deviation} = 44 \ \mu m$$

where

The 95% confidence interval was determined as follows

$$\text{confidence interval} = x_{avg} \pm 1.96 \left(\frac{44}{\sqrt{15}} \right)$$

and Table 9 give the results of the quantitative metallography evaluation and hardness measurements of weld metal and of HAZ of zirconium alloy, respectively. A 95% percent confidence interval was calculated from the standard deviation. The number of hardness indents varied according to the width of the weld. As a consequence, the confidence interval for the hardness was not constant. Underwood equations were used (Equation 1 and Equation 2) to calculate the 95% interval of the percent basket-weave structure. A sample calculation is shown below:

Weld 7 basket-weave structure 95% confidence calculation:

The variance is given by,

$$\left(\frac{\sigma(Pp)^2}{Pp^2} \right) = \frac{1}{P_\alpha} \quad \text{Equation 1}$$

Therefore,

$$\sigma(P_p) = \frac{P_p}{\sqrt{P_\alpha}}$$

Where:

σ^2 is the variance

P_α is the number of points counted in the basket-weave microstructure

P_p point fraction in the basket-weave microstructure

$$\sigma(P_p) = \frac{0.9}{\sqrt{90}}$$

$$\sigma(P_p) = 0.0942$$

The 95% confidence interval is given by,

$$95\% \text{ confidence interval} = 1.96 * \sigma(P_p) \quad \text{Equation 2}$$

$$95\% \text{ confidence interval} = 1.96 * 0.0942$$

$$95\% \text{ confidence interval} = 0.19$$

Weld 7 grain size calculation:

The average of the grain size was determined as follows.

$$\text{average} = \frac{2x(200) + 67 + 9x(100) + 170 + 140 + 190}{15}$$

$$\text{Average} = 125\mu m$$

The standard deviation was calculated as follows.

$$\text{Standard deviation} = \sqrt{\frac{\Sigma(x_i - x_{avg})^2}{(n-1)}}$$

$$\sqrt{\frac{(190-125)^2 + (140-125)^2 + 2x(200-125)^2 + (70-125)^2 + 9x(100-125)^2 + (173-125)^2}{14}}$$

$$\text{standard deviation} = 44 \ \mu m$$

where

The 95% confidence interval was determined as follows

$$\text{confidence interval} = x_{avg} \pm 1.96 \left(\frac{44}{\sqrt{15}} \right)$$

$$\text{confidence interval} = 125 \pm 22$$

Table 7: Summary of the measurements of the width of the weld bead at the top and the bottom surface. The average width is also listed.

Weld no.	Width at top (mm)	Width bottom (mm)	Average width (mm)	Calculated Heat input (J/mm)	Calculated arc efficiency	Cooling rate (°C/s)
1	6.5	5.2	5.8	50	0.11	36
2	7.4	5.9	6.6	60	0.23	28
3	8.0	5.7	6.8	60	0.44	26
4	5.3	2.6	3.9	40	0.27	79
5	10.4	7.5	8.9	80	0.30	15
6	5.2	6.4	5.8	50	0.12	37
7	5.5	3.0	4.2	40	0.24	68
8	3.2	0.0	1.6	10	0.16	480
9	4.8	3.5	4.1	40	0.19	71
10	4.4	3.3	3.8	40	0.19	83
11	8.3	7.2	7.7	70	0.35	20
12	7.2	6.1	6.6	60	0.11	28
13	7.7	6.2	6.9	60	0.32	25
14	3.2	0.0	1.6	10	0.15	480
15	4.4	2.0	3.2	30	0.18	120
16	10.2	8.2	9.2	90	0.31	15
17	10.2	9.8	10.0	90	0.14	12
18	6.7	3.3	5.0	50	0.29	49
19	2.2	1	1.6	10	0.11	480

Table 8: Fraction basket-weave, grain size and hardness of weld metal.

Weld no	Number of point in basket-weave structure	Number of points in parallel plate structure	Fraction Basket-weave	β grain size (µm)	Average Hardness (HV0.3)	No of Hardness indents
1	90	10	0.9±0.19	970±13	167±7	15
2	50	50	0.5±0.15	1380±18	171±7	15
3	100	0	1.0±0.20	1160±15	179±7	11
4	60	40	0.60±0.15	1280±17	169±5	5
5	95	5	0.95±0.19	1530±20	175±11	14
6	80	20	0.80±0.18	1240±16	180±7	15
7	90	10	0.90±0.19	1890±22	175±11	11
8	80	20	0.80±0.18	1130±15	174±11	10
9	80	20	0.80±0.18	1350±18	174±9	9
10	83	17	0.83±0.18	1270±16	169±5	6
11	96	4	0.96±0.19	1140±15	173±4	13
12	80	20	0.80±0.18	1790±23	192±10	5
13	71	29	0.71±0.17	1440±19	171±8	13
14	57	43	0.57±0.15	1230±16	176±6	21
15	82	18	0.82±0.18	1380±18	170±7	5
16	96	4	0.96±0.19	1640±21	174±6	14
17	90	10	0.90±0.19	1770±23	180±6	25
18	95	5	0.95±0.19	1900±25	174±5	16
19	67	33	0.67±0.16	1530±20	161±5	14

Table 9: Fraction basket-weave, grain size and hardness of heat affected zone.

Weld no	Number of point basket-weave structure	Number of Points parallel in plate structure	Fraction Basket-weave	β grain size (μm)	Average hardness (HV0.3)	No of Hardness indents
1	80	20	0.80± 0.18	850 ±11	159± 8	13
2	50	50	0.50± 0.14	1430 ±19	167± 7	12
3	77	23	0.77± 0.17	1270± 17	170± 5	22
4	60	40	0.60± 0.15	880 ±12	162±5	18
5	80	20	0.80± 0.18	1370 ±18	176±3	14
6	85	15	0.85± 0.18	980 ±13	173±7	18
7	95	5	0.95± 0.19	1730 ±23	169±6	23
8	83	17	0.83± 0.18	900 ±12	180±8	14
9	65	35	0.65± 0.16	910 ±12	168±5	19
10	77	23	0.77± 0.17	780 ±10	167±7	14
11	80	20	0.80± 0.18	980 ±130	178±10	11
12	75	25	0.75± 0.17	1690 ±22	176±5	18
13	67	33	0.67±0.16	1240 ±16	172±5	29
14	60	40	0.60±0.15	960 ±13	177±10	9
15	90	10	0.90± 0.19	940 ±12	171±6	19
16	80	20	0.80± 0.18	1470±19	172±6	16
17	87	13	0.87± 0.18	1560±20	176±8	15
18	80	20	0.80±0.18	1640± 22	167±6	9
19	73	27	0.73± 0.17	1260 ±10	158±6	6

6.4 Hardness tests results

The change in hardness across the welded joint was measured for all the nineteen welds. Four welds out of a sample set of 19 successful welds in the matrix were selected to illustrate the general trend in the results of the hardness tests. Welds number 10, 15, 16 and 17 welds were high heat input and low input welds of both pulsed and non-pulsed mode (Appendix A). The hardness measurements were plotted against the distance from the weld centerline. The hardness of the HAZ is similar on the two sides of the weld. The hardness profiles plotted on an absolute distance of welds 10, 15, 16 and 17 are shown Figure 20.

There was no significant difference of the hardness measured on the plane parallel to the surface of the sheet and the hardness measured on the cross-section.
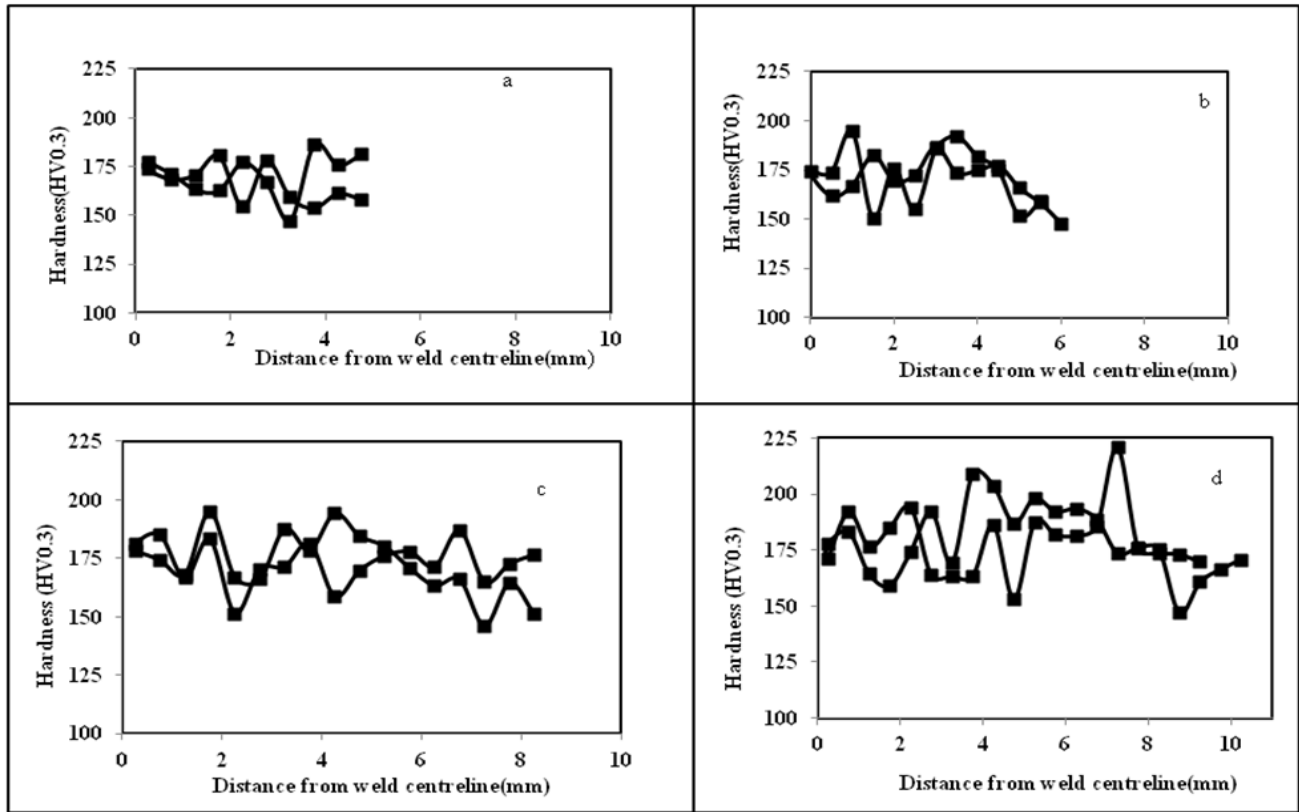
Figure 20:a) Hardness plot of weld 10 (pulsed weld), calculated heat input 40 J/mm, average width of weld was 3.8 mm. b) Hardness plot of weld 15 (non pulsed), calculated heat input of 30J/mm, width of weld was 3.2mm. c) Hardness plot of weld 16 (pulsed), calculated heat input (90J/mm), width of weld was 9.2mm. d) Hardness plot of weld 17(non pulsed), calculated heat input 90J/mm, width of weld was 10mm.

6.4.1 Influence of heat input on hardness

Figure 21 and Figure 22 show that the hardness did not vary significantly with heat input. It can be inferred that pulsed and non-pulsed, high and low heat input did not affect hardness for the given plate thickness. Comparing the hardness of low and high inputs, it is observed that there was no notable difference in hardness values of the weld metal and HAZ. Similarly, there was no difference in hardness values for both weld and HAZ between low and high inputs for pulsed

welds.
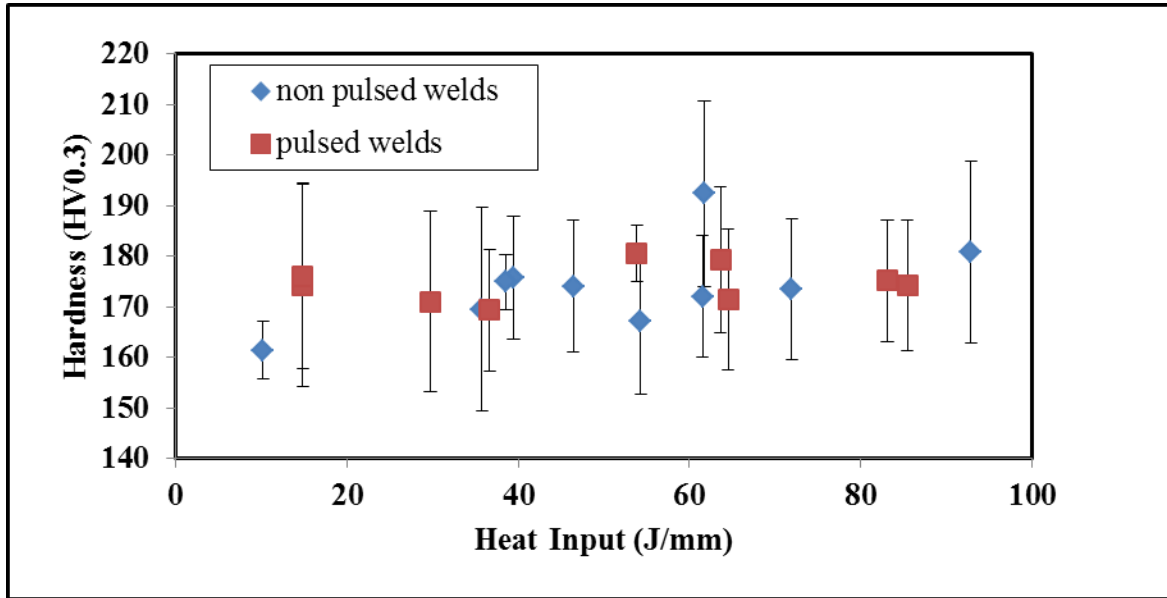
Figure 21: Average weld metal hardness as a function of heat input of all pulsed and non-pulsed current welds. Heat input had no effect on the hardness of the weld metal of zirconium alloy.
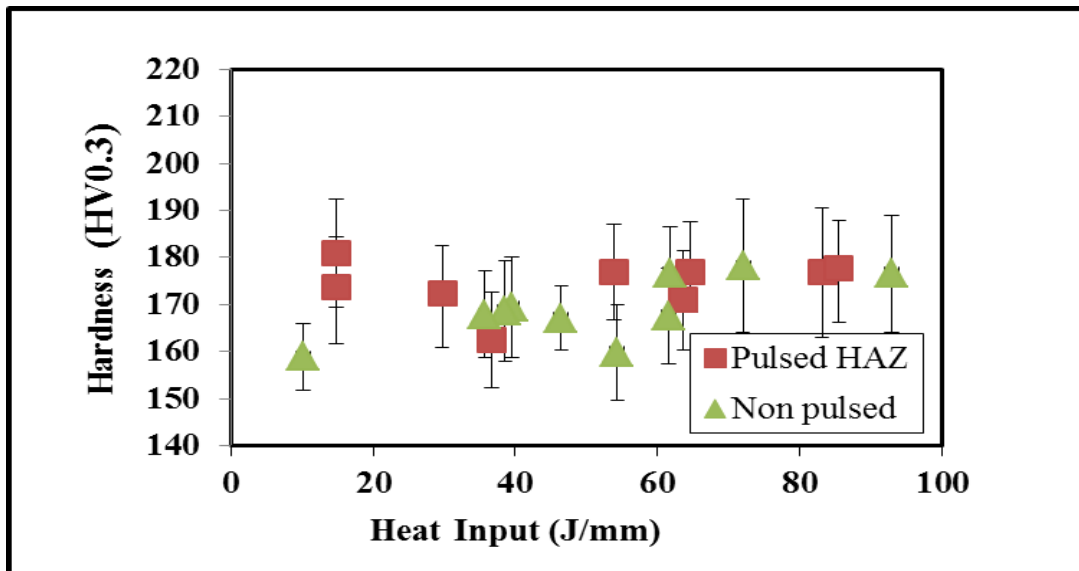
Figure 22: The influence of heat input on hardness of the heat affected zone for all pulsed and non-pulsed current welds. Heat input had no effect on the hardness of the heat affected zone of zirconium alloy.

57

6.4.2 Hardness of welds that showed evidence of gaseous contamination

Table 10 shows the hardness of contaminated welds that is, welds where the flow rate of the trailing gas shield was reduced to a level where gaseous contamination was visible. The average hardness for the contaminated welds, as seen in Table 10, was not significantly different to that of uncontaminated welds. Figure 23 is a visual comparison between a contaminated weld and good weld. Table 11 summarises the hardness measurements, confirming that no difference in hardness between the good welds and contaminated welds could be detected. For contaminated welds 1 and 2, no distinction between weld metal and HAZ could be observed.

Table 10: Summary of the welding parameters for the contaminated welds

	Contaminated weld 1	Contaminated weld 2	Contaminated weld 3	Contaminated weld 4	Contaminated weld 5
Contamina-tion colour	light blue	light yellow	blue	blue	dark blue
Current mode	non-pulsed	pulsed	non-pulsed	pulsed	non-pulsed
Heat input	47.3 J/mm	12.6 J/mm	52.5 J/mm	97.9 J/mm	71.5J/mm
Average hardness of weld metal and HAZ	170 HV0.3	156 HV0.3	159 HV0.3	173 HV0.3	179 HV0.3
Number of hardness measurements	17	15	28	34	30
weld metal hardness	Fusion line not distinguishable	Fusion line not distinguishable	162 ± 6 HV0.3	168± 9 HV0.3	200± 3 HV0.3
HAZ Hardness			156 ±7 HV0.3	177±12 HV0.3	162± 6 HV0.3

Table 11: Comparison of non-contaminated and contaminated welds hardness.

Type of weld	Average weld metal hardness	Average HAZ hardness	Average hardness of base metal
No visual evidence of contamination (19 welds, 237 measurements)	174±3	170±3	184±4
Visual evidence of contamination present (5 welds, 69 measurements)	171±14	166±10	

a)   b)
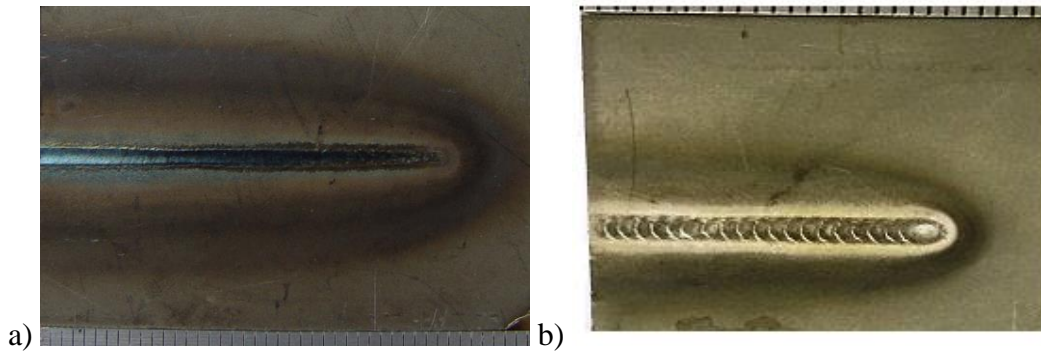
Figure 23: a) Image of contaminated weld 1, heat input 13 J/mm, with an average hardness of 170 HV0.3 b) Image of weld 14 (good weld), calculated heat input of 10 J/mm with average hardness of 177 HV0.3.

6.5 Microstructural evaluation of the welded joint

6.5.1 Microstructure at the centerline of the weld

Welds 10, 15, 16 and 17 microstructures are shown below in Figure 24, Figure 25, Figure 26 and Figure 27, respectively. It is clearly observed that the parallel plates structure nucleated from prior beta grain boundaries, as seen on Figure 26. No martensite was observed in the weld metal. The welds have a high percentage of fine basket-weave structure on the weld center.

Figure 24: Weld metal microstructure of weld 10, showing fine prior beta grains at x20, 40J/mm heat input, 83% basket-weave and 1270±16 μm β grain size. The microstructure was a mixture of basket-weave and parallel plate.
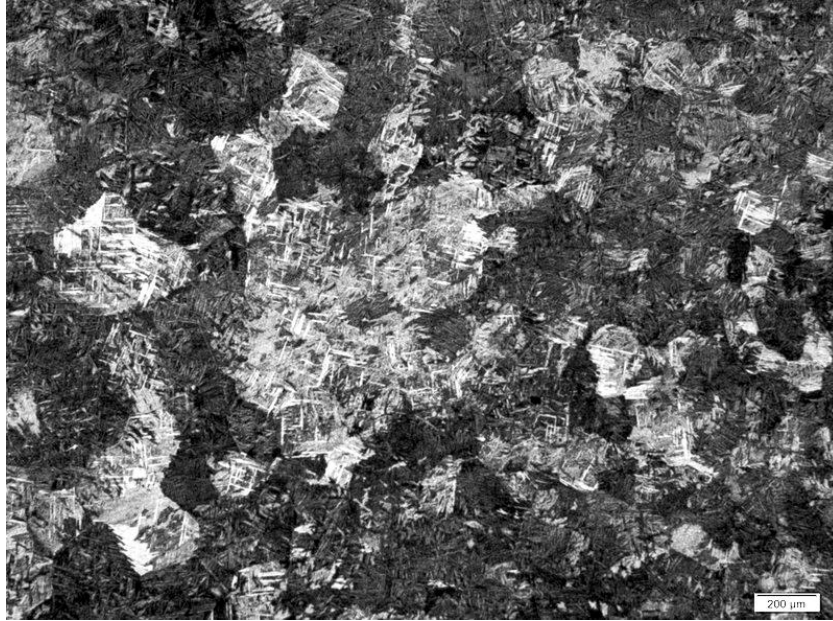
Figure 25: Weld metal microstructure of weld 15, showing coarse prior beta grains x20, 30 J/mm heat input, 82% basket-weave and 1380±18 μm β grain size. The microstructure was a mixture of basket-weave and parallel plate.

Figure 26: Weld metal microstructure of weld 16 showing coarse prior beta grains at x20, 90J/mm heat input, 96% basket-weave and 1640±21 μm β grain size. The microstructure was predominantly basket-weave.
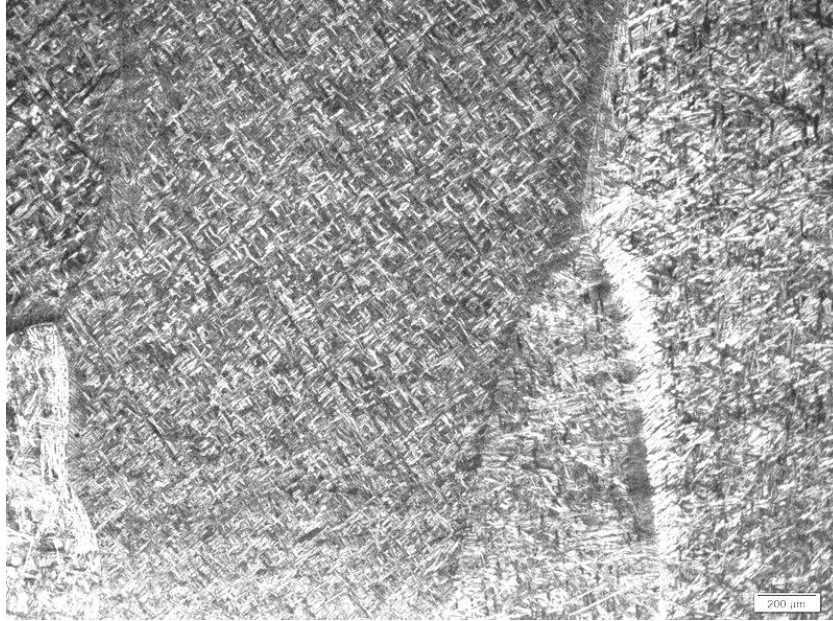
Figure 27: Weld metal microstructure of weld 17, showing coarse prior beta grains at x 20, 90J/mm heat input, 90% basket-weave and 1770±23 μm β grain size. The microstructure was predominantly basket-weave.

6.5.2 HAZ microstructure

The HAZ of zirconium for both non-pulsed and pulsed showed fine prior beta grains for low heat input and coarse prior grain size at high heat input, as shown in Figure 28, Figure 29 and Figure 30. The HAZ also has a high percentage of basket-weave structure. Figure 31 shows a plot of prior beta grain size of both pulsed and non-pulsed welds, as well as, heat input.

Figure 28: HAZ microstructure of weld 10 showed fine prior beta grain at x20, 40 J/mm heat input, 77% basket-weave structure and 780±10 µm β grain size. The microstructure was a mixture of basket-weave and parallel plate structure.

Figure 29: HAZ microstructure of weld 15 showed fine prior beta grain at x20, 30J/mm heat input, 90 %basket-weave structure and 940±12 µm β grain size. The microstructure was a mixture of basket-weave and parallel plate structure.

Figure 30: HAZ microstructure of weld 16 showed fine prior beta grain at x20, 90J/mm heat input , 80% basket-weave structure and 1470±19 μm β grain size. The microstructure was a mixture of basket weave and parallel plate structure.
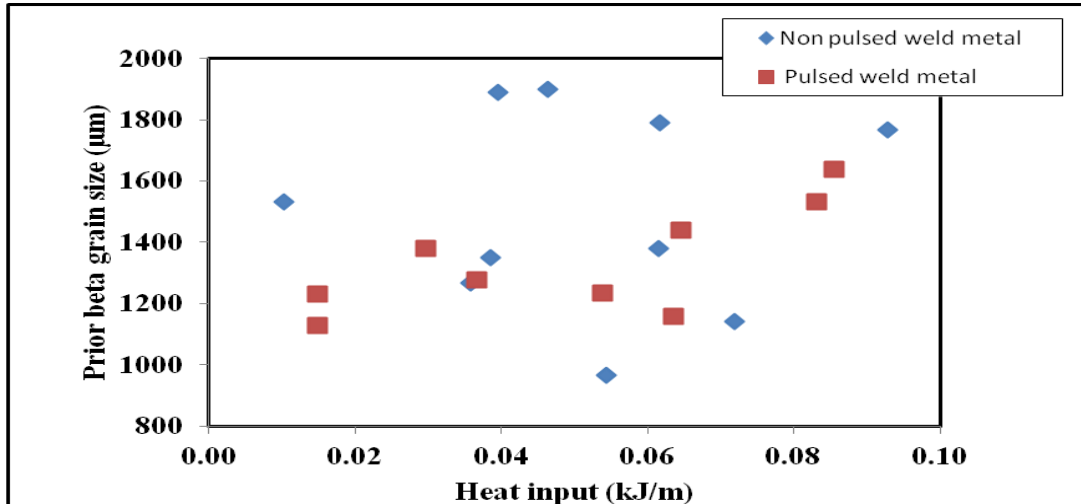
Figure 31: Prior β grain sizes of the weld metal for both pulsed and non-pulsed welds increase with increasing heat input. The prior β grain size of the pulsed welds increases with an increase in heat input. The prior β grain size of the non-pulsed welds was not particularly sensitive to heat input.

6.5.3 Microstructural comparison between planar view and cross section view

Figure 32 shows a predominately basket-weave microstructure of weld metal with fraction basket-weave of 0.85. The weld metal microstructure seen in Figure 32 was taken on the planar view.

Figure 32: Planar view of weld 14, weld metal microstructure (10 J/mm) showing a predominately basket –weave microstructure (fraction basket-weave is 0.85).

Figure 33 shows a predominately basket-weave microstructure of weld metal with fraction basket- weave of 0.90. The weld metal microstructure seen in Figure 33 was taken on the cross section view of the sample. The percent basket-weave structure observed on both planar and cross section views of the weld 14 are consistent. The β grain size of the two polished sections were similar.
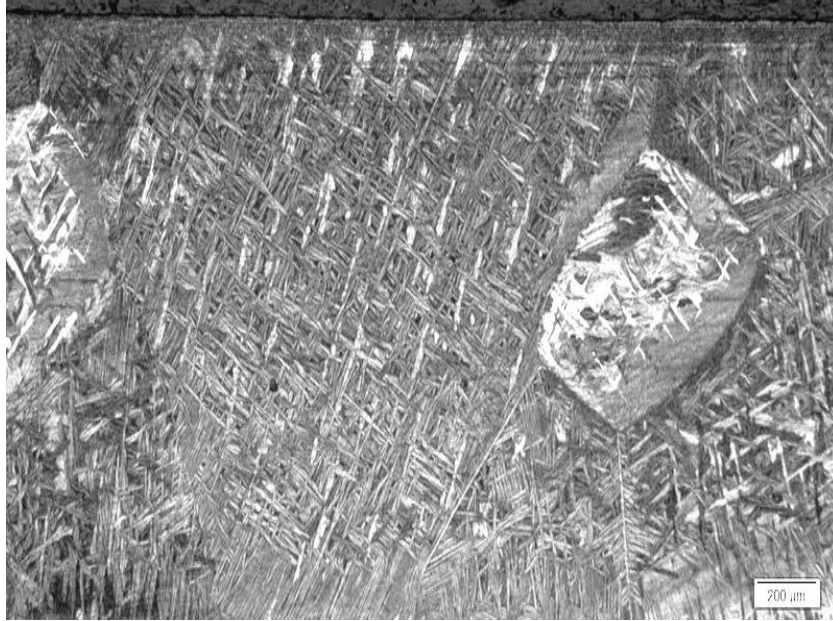
Figure 33: Cross section view of weld 14, weld metal microstructure, 10 J/mm, performed using pulsing showing a predominately basket–weave microstructure (fraction basket weave is 0.90).

6.5.4 Contaminated weld metal and HAZ

The contaminated weld metal and HAZ microstructures can be seen in Figure 34 and Figure 35 There was no notable difference in microstructure of the welded joint between the contaminated welds and non-contaminated welds.
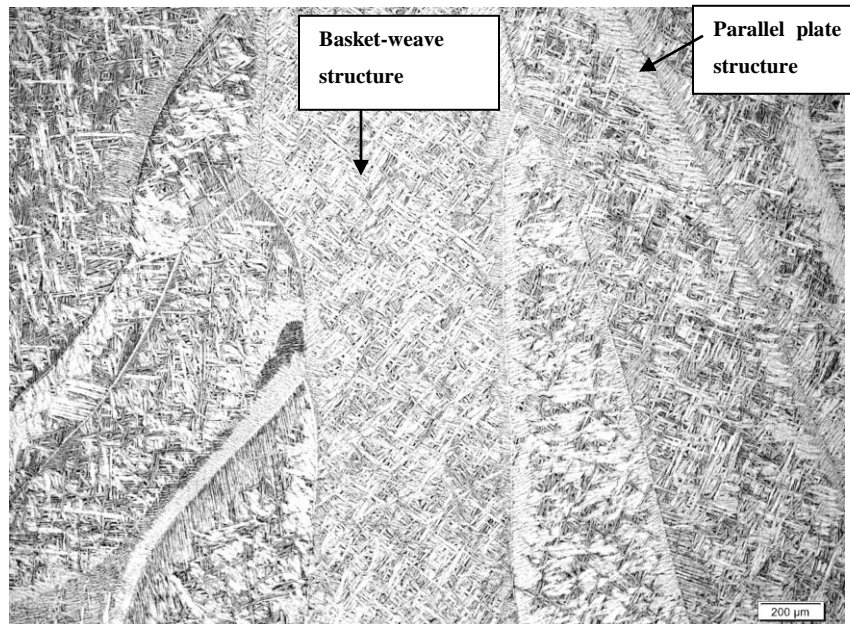
Figure 34: Microstructure of weld metal 3, 52.5J/mm heat input, performed with pulsed current showing coarse grain sizes. The average hardness of the contaminated pulsed weld was 159 HV0.3.

Figure 35: Microstructure of HAZ 3, 52.5J/mm heat input, performed with pulsed current showing coarse grain sizes. The average hardness of the contaminated pulsed weld was 159 HV0.3.

6.5.5 Comparison of hardness of welded joints and dilatometry samples

The cooling rate of the weld and dilatometry samples ranged from 12°C/s to 480°C/s and 10°C/s to 600°C/s, respectively. It was observed that the percentage basket-weave structure of the weld metal and HAZ was not sensitive to the cooling rate. In contrast, the percentage basket-weave structure in the dilatometry samples increased with the cooling rate, as shown Figure 36. It was observed that hardness was not sensitive to percentage basket-weave structure for both weld and HAZ as seen in Figure 37.

Hardness was not sensitive to percentage basket-weave structure for dilatometry samples, as shown in Figure 37. The weld metal and HAZ hardness was not sensitive to the cooling rate but the dilatometry samples show an increase of hardness with basket-weave structure, as shown on Figure 38. The fraction basket-weave structure in the dilatometry samples increased with an increase in cooling rate. Also, for most welds, the fraction basket-weave structure in the HAZ was approximately similar to the fraction basket-weave in a dilatometry sample that had been subjected to a similar cooling rate (see Figure 36).

68
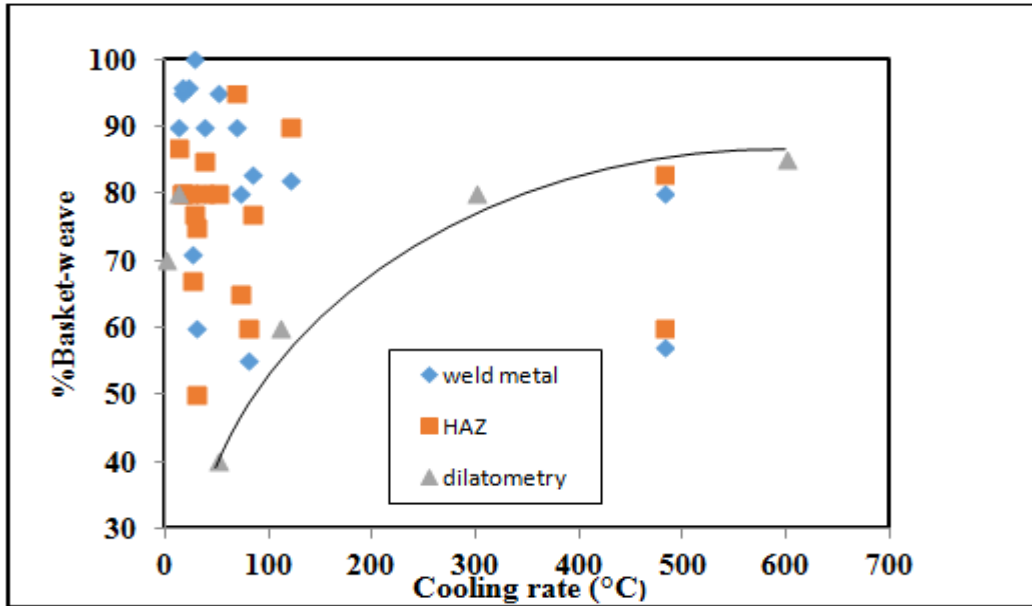
Figure 36: The influence of the cooling rate on fraction basket-weave for weld metal, HAZ and dilatometry samples. The percentage basket-weave structure in the dilatometry samples increased with the cooling rate
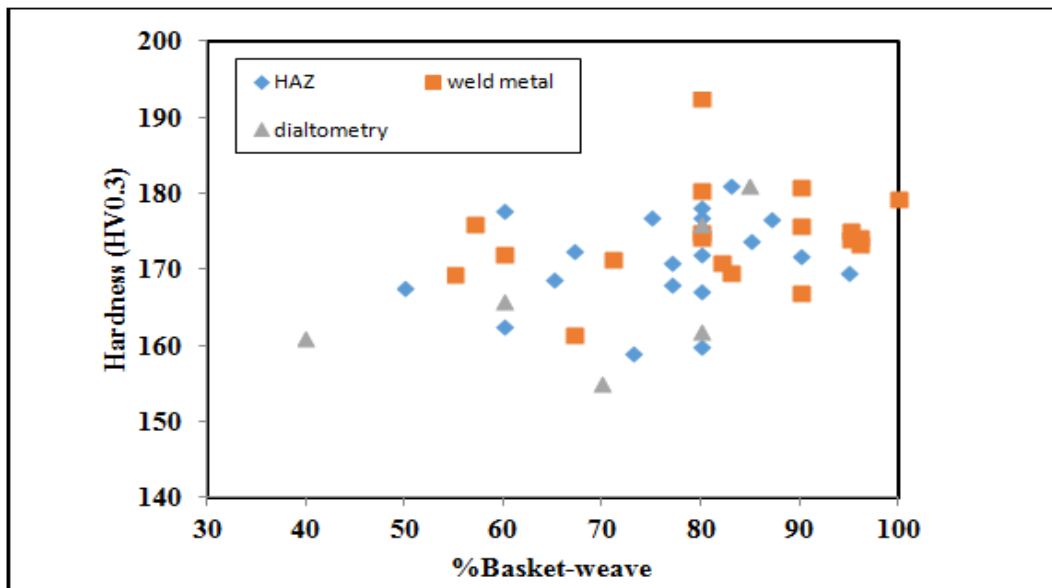
Figure 37: The influence of percentage basket-weave structure on hardness for weld metal, HAZ and dilatometry. The hardness was not sensitive to percentage basket-weave structure for both weld and HAZ
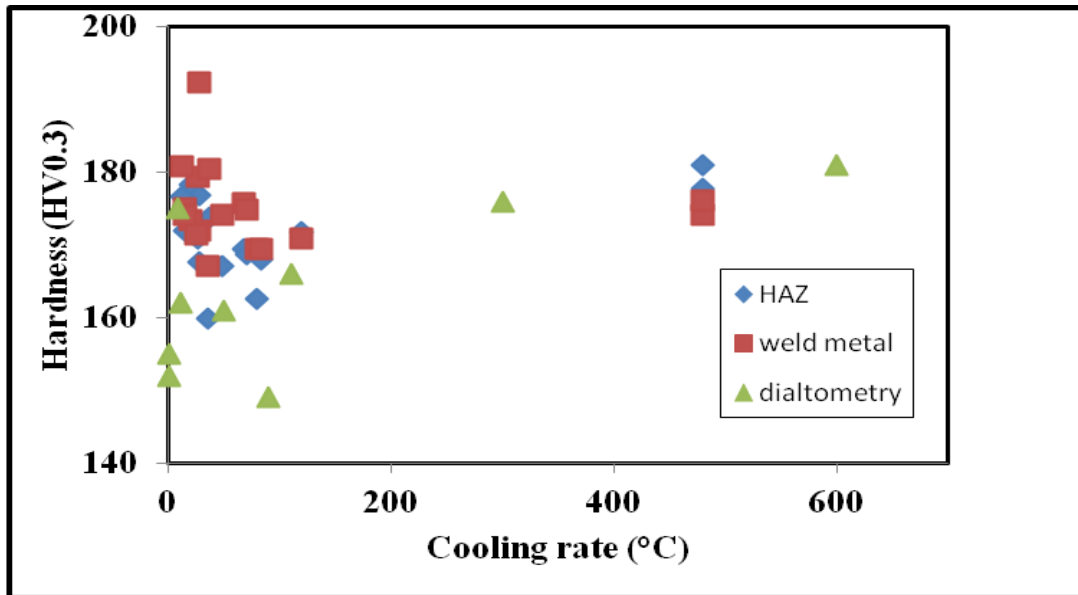
Figure 38: **The influence of the cooling rate on hardness for weld metal, HAZ and dilatometry.**

Hardness was not sensitive to beta grain size for both the weld metal and HAZ, as seen in Figure 39. This result was consistent with the observation of Figure 38. The prior β grain size was not sensitive to the cooling rate for weld metal and HAZ, as seen on Figure 40.

The percentage basket-weave structure was not sensitive to β grain size, as seen in Figure 41. As basket-weave nucleates inside the β grain[7], it was expected that the fraction basket-weave structure would be insensitive to the β grain size. As the prior beta grain size of the weld metal increased, the fraction basket-weave microstructural constituents increased, for pulsed welds. Moreover, if no pulsing was used, the weld metal showed β grain size showed more scatter. See Figure **42**. Figure 42 also shows that the microstructure of the pulsed welds was not significantly finer than that of the non pulsed welds but made a more predictable outcome correlation with grain size.
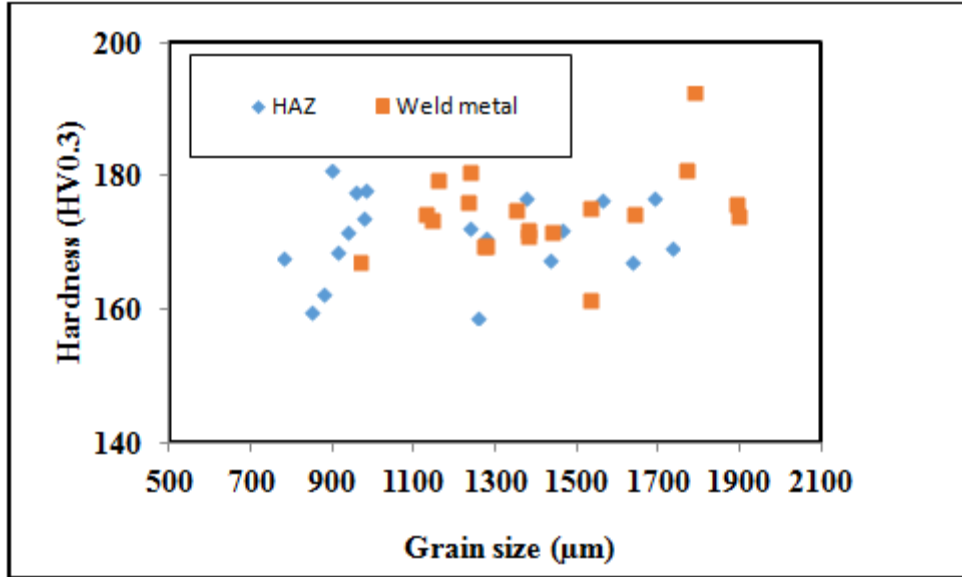
Figure 39: The influence of prior β grain size on the hardness for weld metal and HAZ. The hardness of the weld metal and HAZ was not sensitive to grain size for combined weld pulsed and non-pulsed, as well as, weld metal and HAZ.
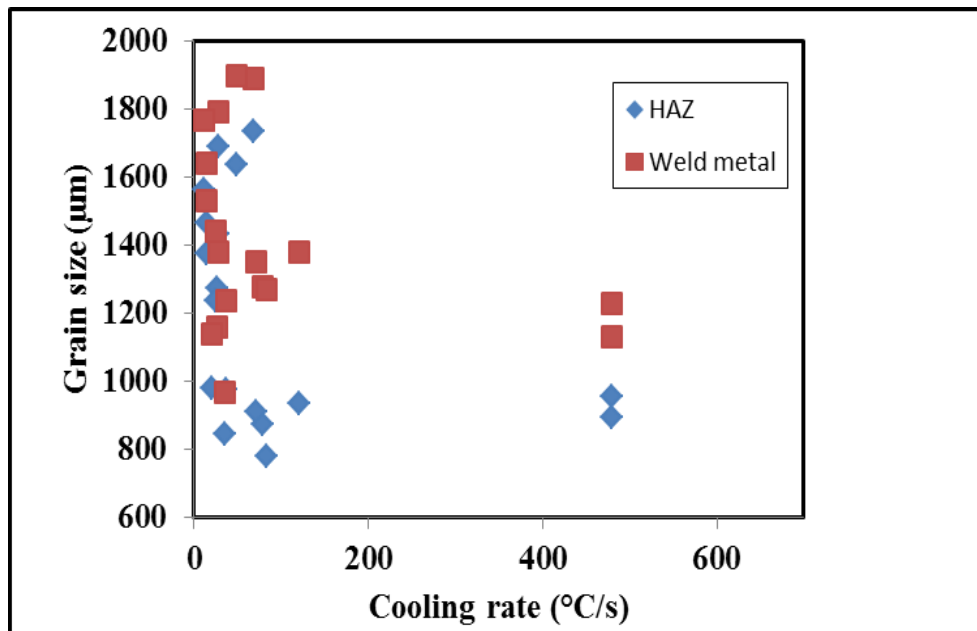
Figure 40: The influence of cooling rate on β grain size. The prior β grain size was not sensitive to the cooling rate for weld metal and HAZ.

71
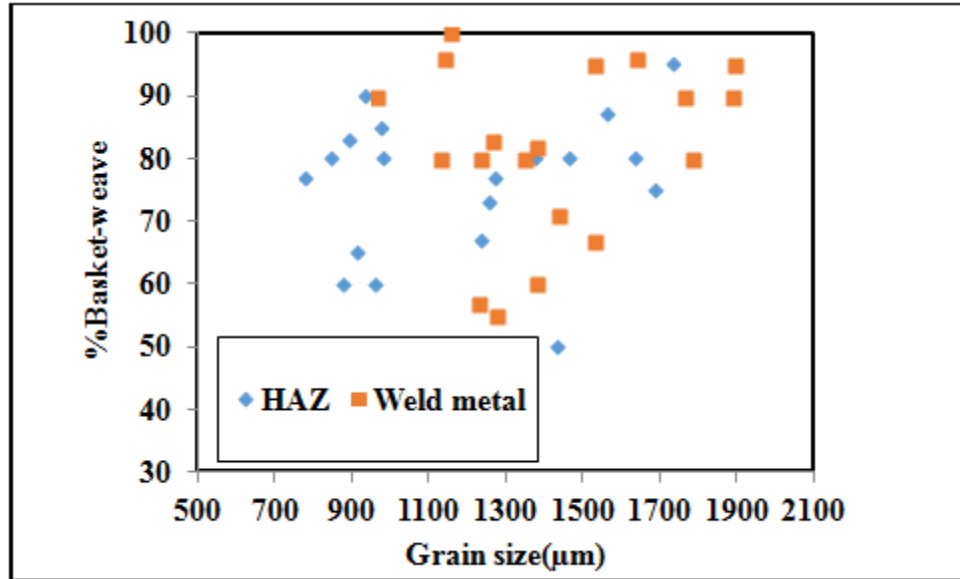
Figure 41: The influence of β grain size on percentage basket-weave structure. The percentage basket-weave structure was not sensitive to β grain size, for combined weld pulsed and non-pulsed, as well as, weld metal and HAZ.
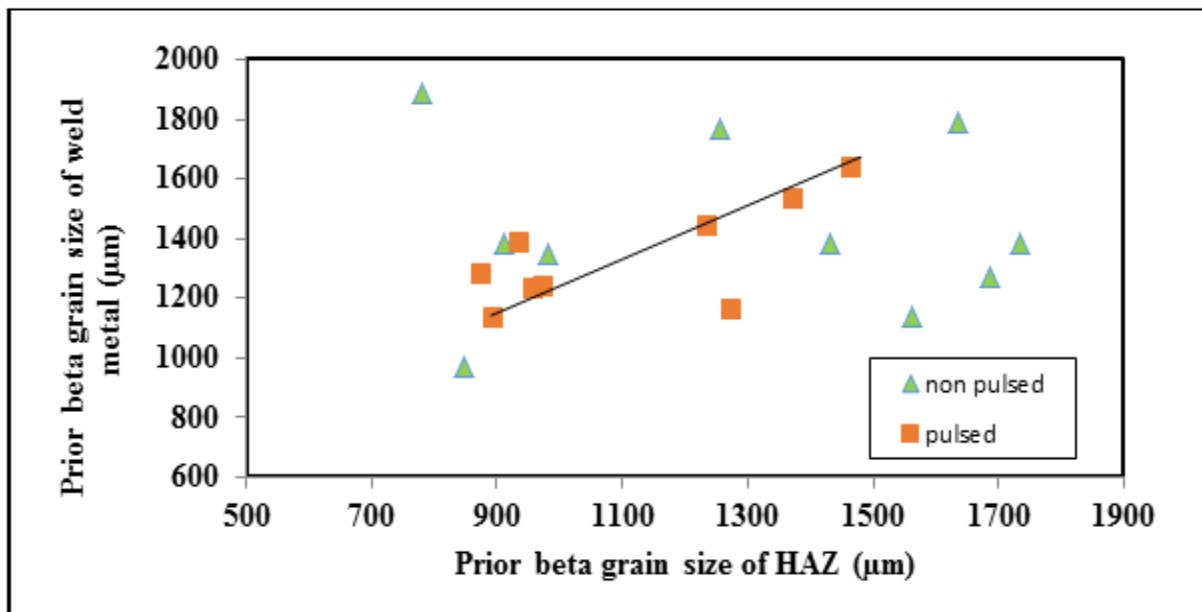
Figure 42: Change of weld metal grain size with HAZ grain size. The microstructure of the pulsed welds was not significantly finer than that of the non pulsed welds but made a more predictable outcome correlation with grain size

72

6.6 Results of dilatometry evaluation

The phase transformation from alpha to beta, on heating, and beta to alpha, on cooling, in the annealing cycle with a peak temperature of 1100°C, can be seen in Figure 43. The second heat treatment cycle simulates a weld thermal cycle. The transformation start and transformation end temperatures are shown in Table 12. The heat treatment cycle of dilatometry sample, D4, is shown on Figure 43. The dilatometry sample D4 was cooled at a rate of 1.1°C/s. From Figure 43 it can be seen that the annealing cycle was not necessary as the phase transformation behavior during the annealing cycle was identical to phase transformation behavior during the weld simulation cycle.

Table 12, below, shows the hardness and quantitative metallography data for the dilatometry samples. The transformation start and end temperature for alpha to beta transformation at different cooling rates are summarized as well as, the percentage basket-weave structure. The average hardness of all the dilatometry samples was 164±4 HV which was similar to that of the hardness of the HAZ (170±3HV).

The transformation temperatures were determined using the approach reported by Atkins [29] as shown on Figure 44. Figure 45 shows the heating curves with the actual transformation start temperatures and transformation end temperatures superimposed. It can be seen that the alpha to beta transformation started below 900°C but did not go to completion for dilatometry samples with a peak temperature of 900 °C.

Figure 46 shows the cooling curves with the actual transformation start temperatures and transformation end temperatures superimposed. From Figure 46, it can be seen that the transformation end temperature, on cooling, was below 900 °C for dilatometry samples that have a peak temperature of 900°C. Figure 47 shows the continuous cooling transformation (CCT) diagram. The curves shown in Figure 45and Figure 46 were adjusted with an arbitrary offset to separate the individual curves.
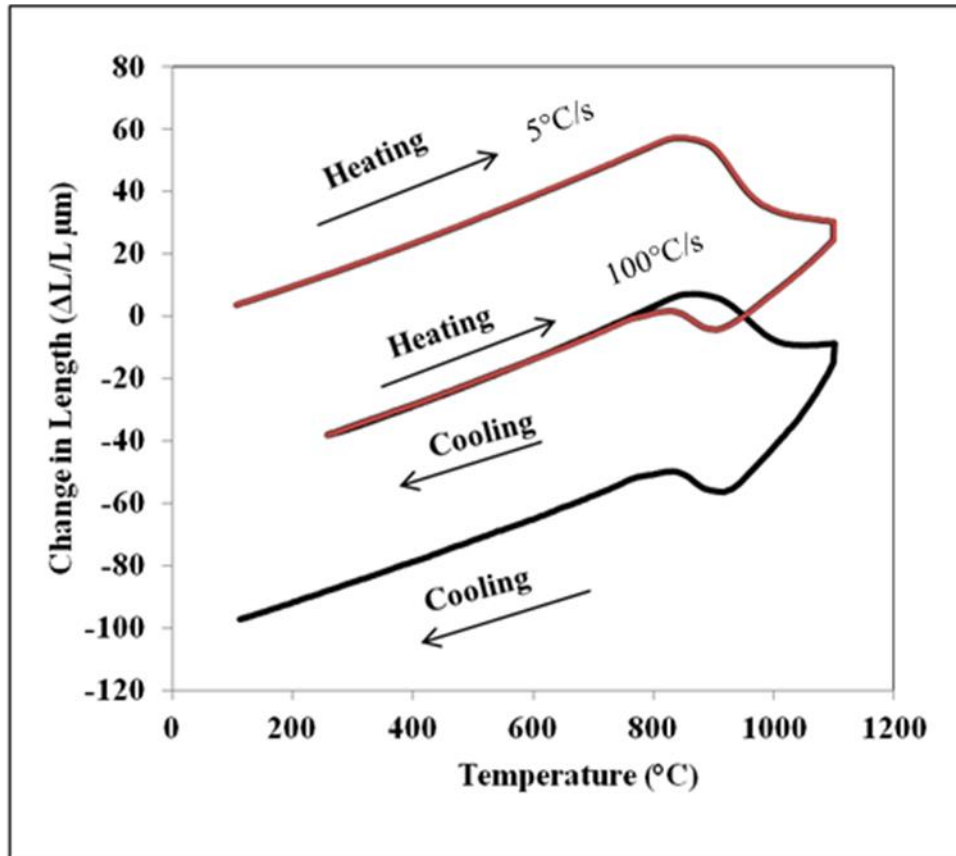
Figure 43: Full dilatometry heat treatment cycle. Two transformation cycles can be seen on the heat treatment cycle of D4, at a cooling rate of 1.1°C/s.
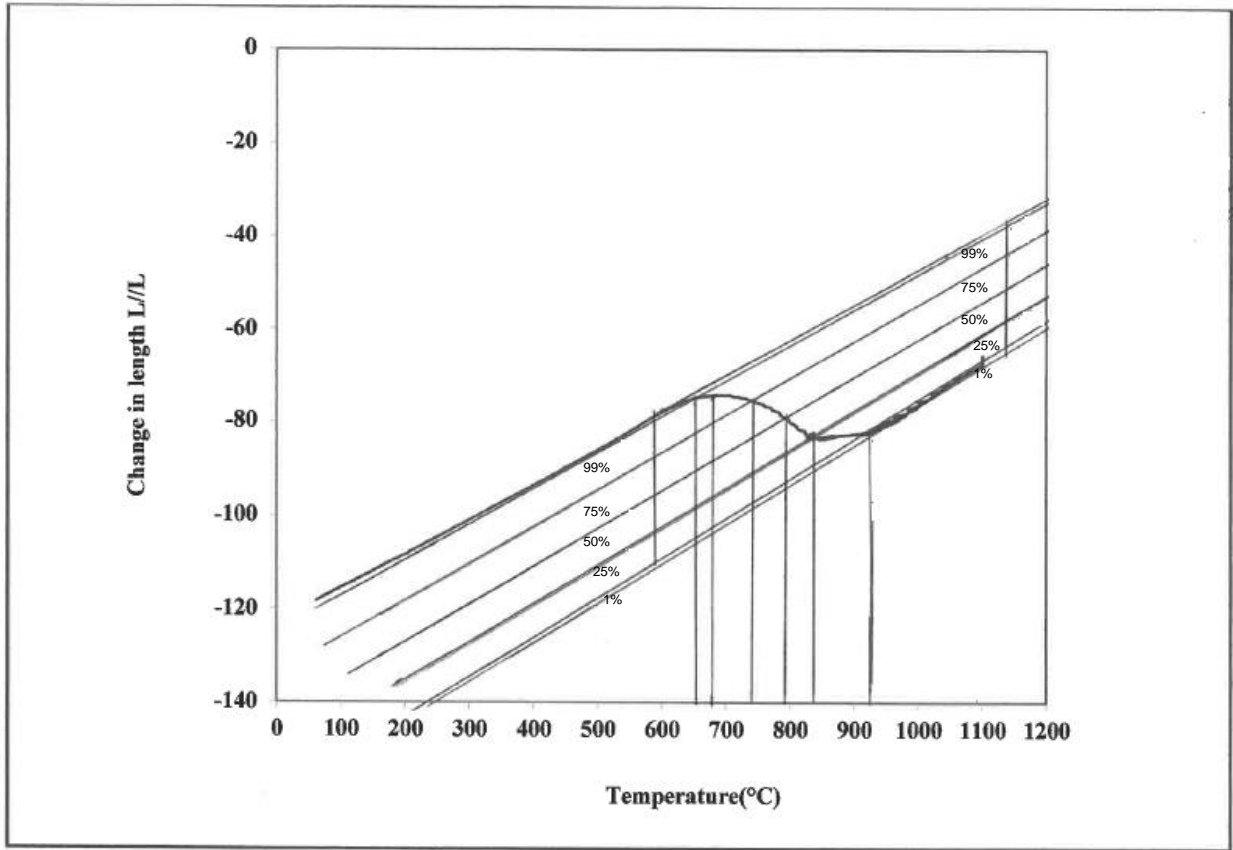
Figure 44: Illustration of the determining of transformation temperature using Atkin approach

Table 12:Transformation start and end temperature for dilatometry samples.

| Dilatometry No | Heat treatment cycle | | | | On Heating | | On Cooling | | % Basket - weave | Hardness |
	1st Peak Temp °C	2nd Peak Temp °C	Cooling rate °C/s	$\Delta t_{9\text{-}5}$ (s)	Transformation start °C	Transformation end °C	Transformation start °C	Transformation end °C		Average (HV)
D4	1100	1100	1.1	273	813	1004	934	801	70	155±4.
11°C	1100	1100	11	27	836	1030	915	701	80	162±4.
Dc3	1100	1100	110	3	808	1008	915	647	60	166±5
50°C	1100	1100	50	6	832	1051	908	677	40	161±4
300.	1100	1100	300	1	833	1071	896	677	80	176±4
600	1100	1100	600	1	812	1071	838	676	85	181±5
UC51	1100	900	0.9	333	834	N/A	N/A	786	N/A	152±8
UCD2	1100	900	9	33	807	N/A	N/A	786	N/A	175±8
CD2	1100	900	90	3	826	N/A	N/A	718	N/A	149±3
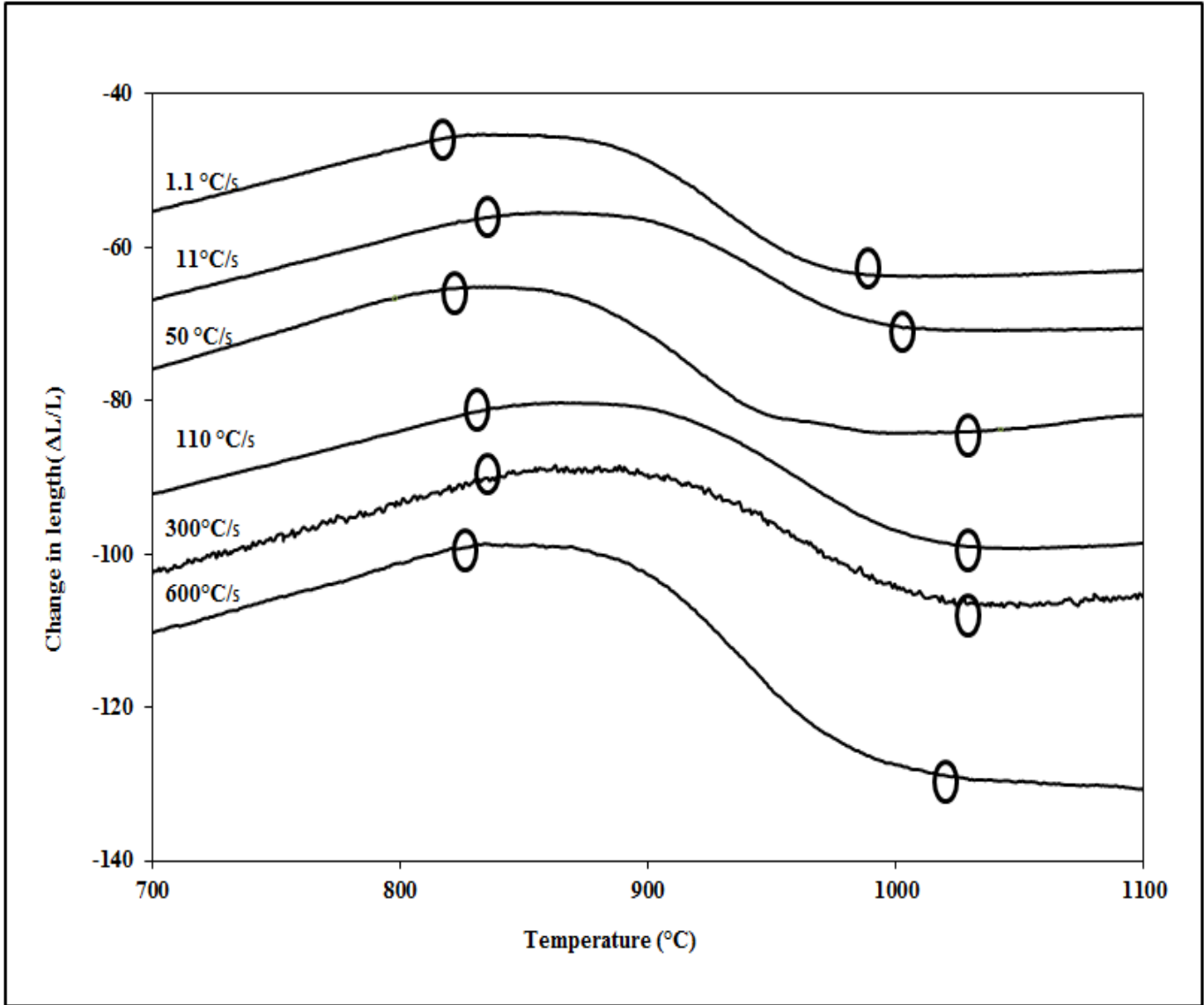
Figure 45: Dilatometry heating curves from 200 °C to either 900°C or to 1100 °C with transformation start and end temperatures on heating noted. Individual curves are identified by the subsequent cooling rate. The average transformation start on heating was 822± 8°C and the average transformation end on cooling is 1039°± 24°C.
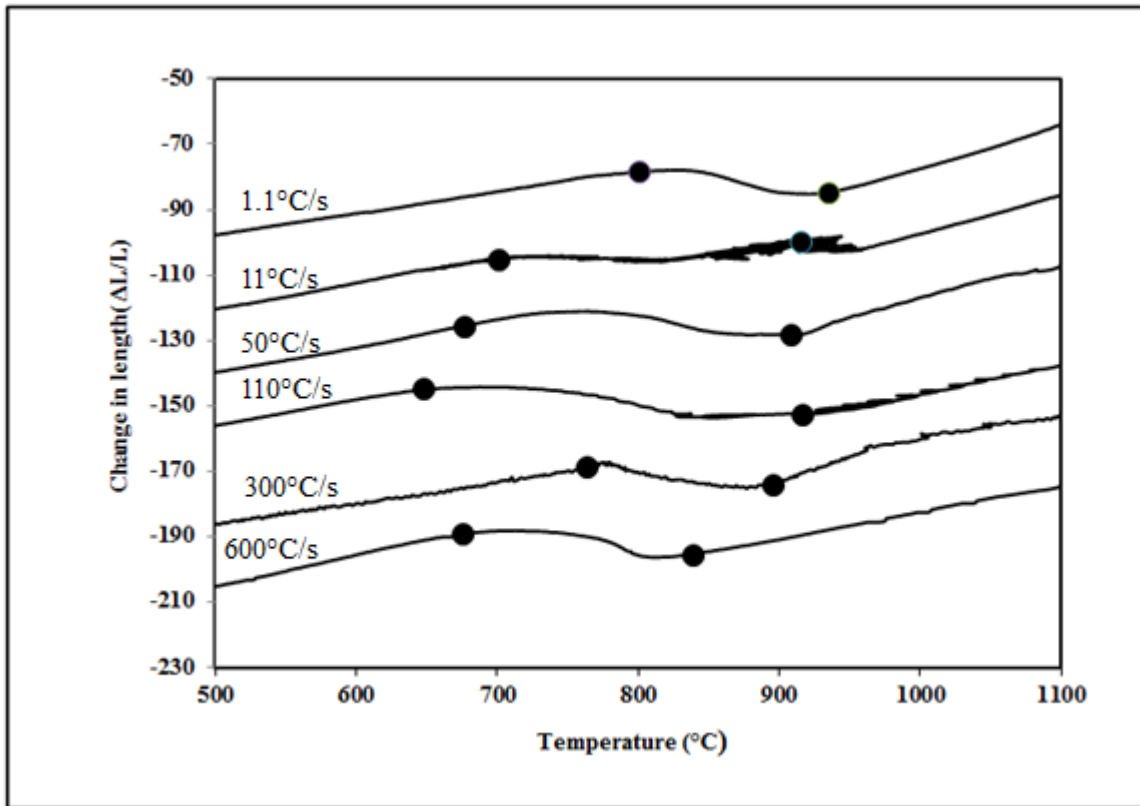
Figure 46: Cooling curves of dilatometry samples (transformation start and end temperatures noted as circles on a curve) for the different cooling rates. Transformation start is taken as 1 % of transformation on cooling and transformation end is taken as 99% of transformation on cooling.
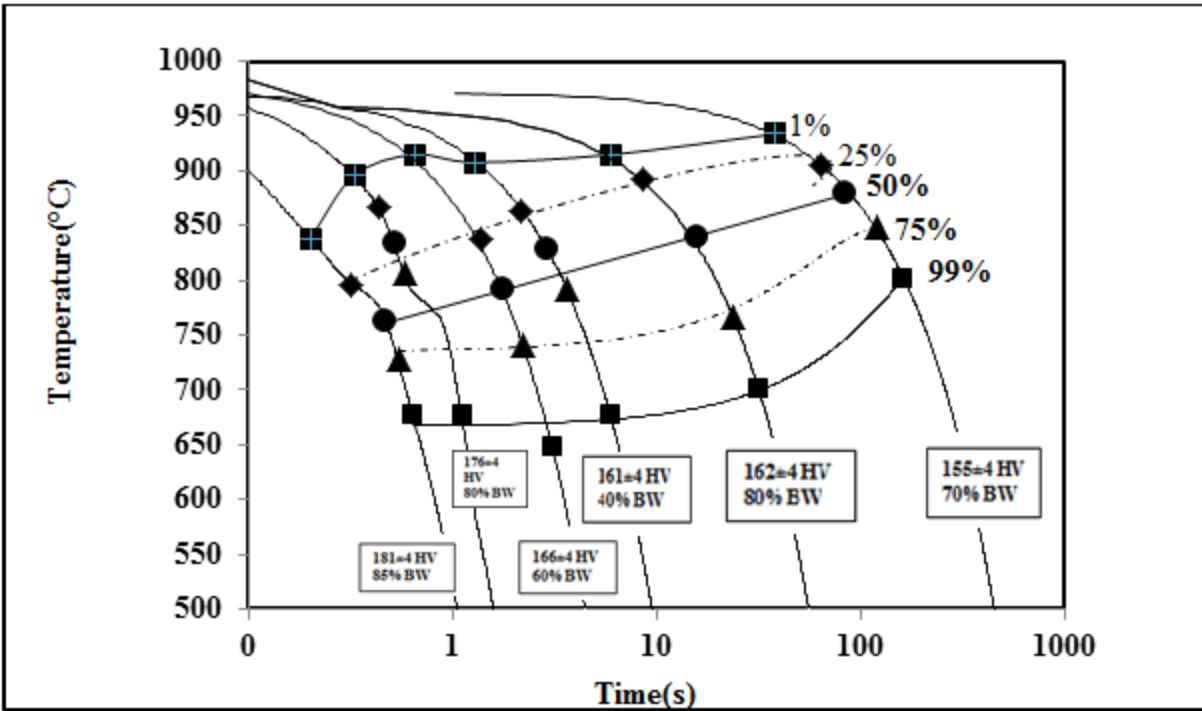
Figure 47: Continuous cooling transformation diagram of the dilatometry samples showing the transformation start and end temperature at different cooling rates from a peak temperature of 1100⁰C. Cooling rates varied from 1.1 to 600⁰C/s.

6.7 Transmission Electron Microscope images of second phase particles

The transmission electron microscope experiment was conducted at the HRTEM unit in Nelson Mandela Metropolitain University (NMMU). The TEM samples were prepared with Helios Nanos Nanolab 650 FIB -SEM. A JEM -2100 (LaB 6). Sample preparation for transmission electron microscopy entailed four steps:

(i) deposition of a protective layer of platinum onto the specimen surface in the selected area,

(ii) extraction and rotation of the wedge containing the selected area,

(iii) removal of the protective material and

(iv) the final cleaning step.

Transmission electron microscopy was used to investigate the presence of second phase particles. Second phase particles were found on the base material along grain boundaries and at triple points, as seen on Figure 48. No second phase particles were observed in the weld metal or in the heat affected zone. It is, however, not conclusive that second phase particles were not present in the heat affected or the weld metal as the Transmission Electron Microscope sample originated from a small part of the welded joint.
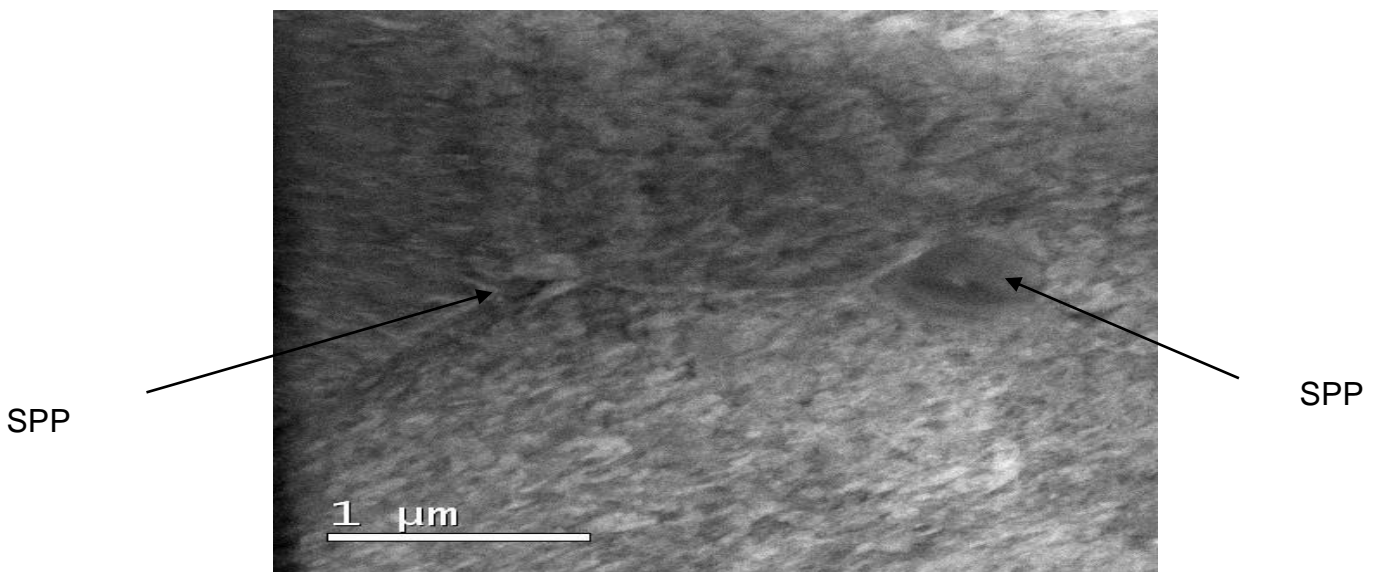
Figure 48: Transmission Electron Microscope (TEM) image of the base material of weld no 13 showing second phase particles (denoted SPP) along a β-βgrain boundary and at a triple point.

6.8. Summary of observations

From the various results presented in this chapter, the following are considered to be the main observations of the current study:

- The range of the arc efficiency was 0.11 to 0.44, consistent with published results.

- The hardness did not vary with the heat input for both welding modes. The hardness of the HAZ was similar on the two sides of the weld.

- The percentage basket-weave structure was not sensitive to the cooling rate for both weld metal and β grain size increased with $\Delta t_{9\text{-}6}$ for pulsed welds and a scatter for non-pulsed welds was observed. Hardness was not sensitive to the percentage of basket-weave structure for weld metal and HAZ for both welding modes.

- The percentage basket-weave structure increases with an increase in cooling rate and hardness for dilatometry samples. Dilatometry results are consistent with the HAZ results.

- Second phase particles was observed in the base material but not in the weld metal or HAZ.

Chapter 7: Discussion

7.1 Base metal

The chemical composition of the base metal complies with the specification of Zircaloy- 2 with the exception of the nickel content. The nickel specification limit in Zircaloy-2 is 0.03-0.08%. No nickel was detected in the base material of this investigation. The addition of nickel was to improve the corrosion properties of Zircaloy-2[3] The by-product of this addition was the formation of second phase particles. The absence of nickel does not affect the mechanical properties but rather the corrosion properties. The absence of nickel was therefore not considered to be crucial to the findings of this study. The thickness of the base metal 1.2 mm. The base metal hardness was 184±4 HV0.3.

7.2 Welding of zirconium - practical considerations

Good welding of zirconium alloy was achieved through good purging. It was found that a combined argon flow rate of 15 liters/min for backing plate and trailing gas shield was optimum. Excessive purging flow rates led to an unstable arc thus, there will be a lack of fusion problems. A precise welding fixture helps keep air from contaminating the sample during welding. It was found that having a longer after flow time compared to pre-flow time avoided the weld from being oxidised. The welds complied with SANS15614-6 and the requirements for the visual appearance, as noted by Ettienne.[2]

7.3 The welding matrix investigated

7.3.1 Region of feasible welds

The welding matrix was used to show the heat input limits of zirconium 1.5%Sn at a thickness of 1.2 mm (see Figure 12). The limits ranged from burn through to no fusion using pulsed and non-pulsed current. Above a current of 94 A, the sample indicated burn through, moreover, a current of 35 A and below indicated an unstable arc and arc initiation problems occurred. No fusion occurred at a welding speed above 5 mm/s.

The estimated arc efficiency ranged between 0.11 and 0.44 (see Appendix A). The median and the average of all the arc efficiencies were 0.19 and 0.22, respectively, as seen in Figure 18. Arc efficiencies cited in the literature are range from 0.22 to 0.80. The estimated arc efficiencies reported in this study were, therefore, consistent with the published values.

7.3.2 Mapping of metallurgical and mechanical response to the welding matrix

The pulsed and non-pulsed welds have similar metallurgical and mechanical responses.

- A map of the weld metal grain size response to the welding matrix parameter is seen in Figure 49. A grain size value of 1500µm was chosen as it was an average grain size value.

- A map of the weld metal hardness response to the welding matrix parameter is seen in Figure 50. A hardness value of 170HV was chosen as it was an average hardness value.

- Figure 51 shows a map of the percent basket-weave on the welding matrix. A percent basket-weave of 0.8 was chosen as it was an average value.

From Figure 49, Figure 50 and Figure 51, it can be inferred that the mechanical and metallurgical responses of zirconium 1.5%Sn were not affected by β grain size, percentage basket-weave or hardness in the region of welds. Therefore, for zirconium 1.5%Sn with a thickness of 1.2mm, considering the welding parameters investigated, the mechanical and metallurgical properties of the 19 successful welds were essentially constant over the range of welding parameters evaluated. No similar published work detailing the effect of heat input on the weld metal and HAZ was found in literature.
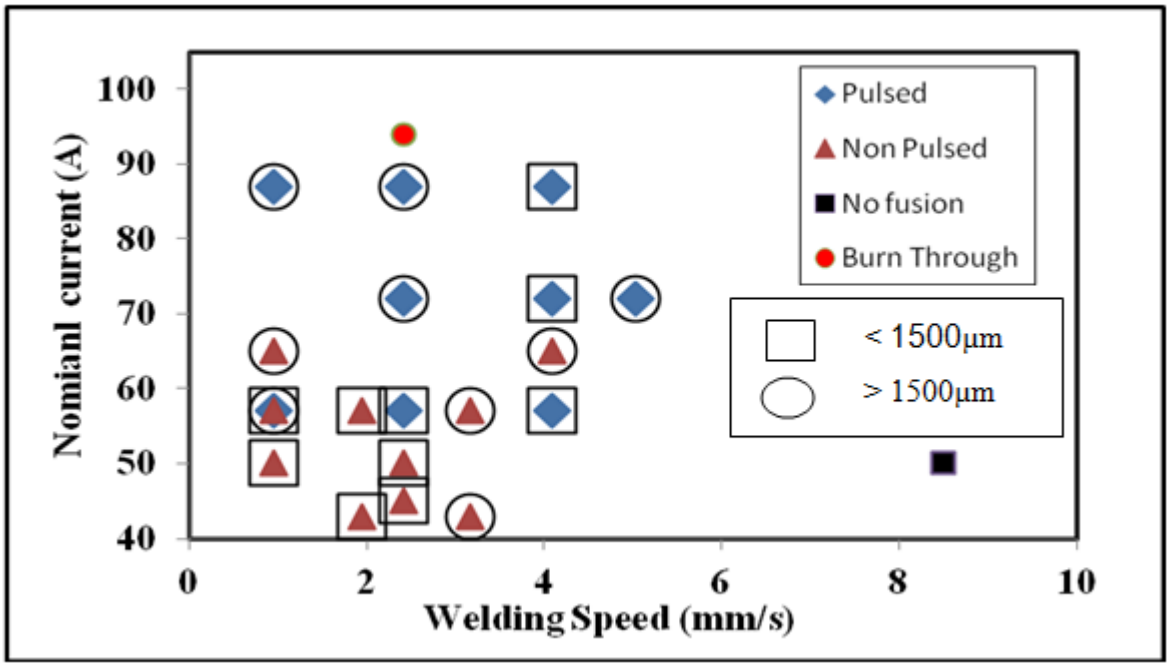
Figure 49: A map of β grain size of the weld metal on the welding matrix.
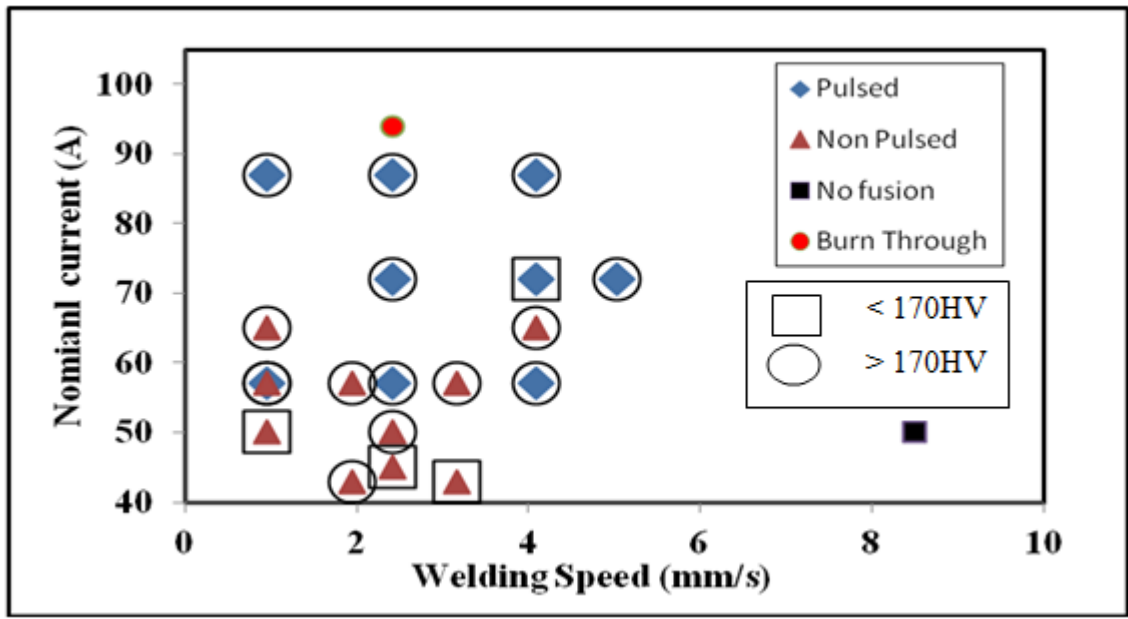
Figure 50: A map of the weld metal hardness on the welding matrix.
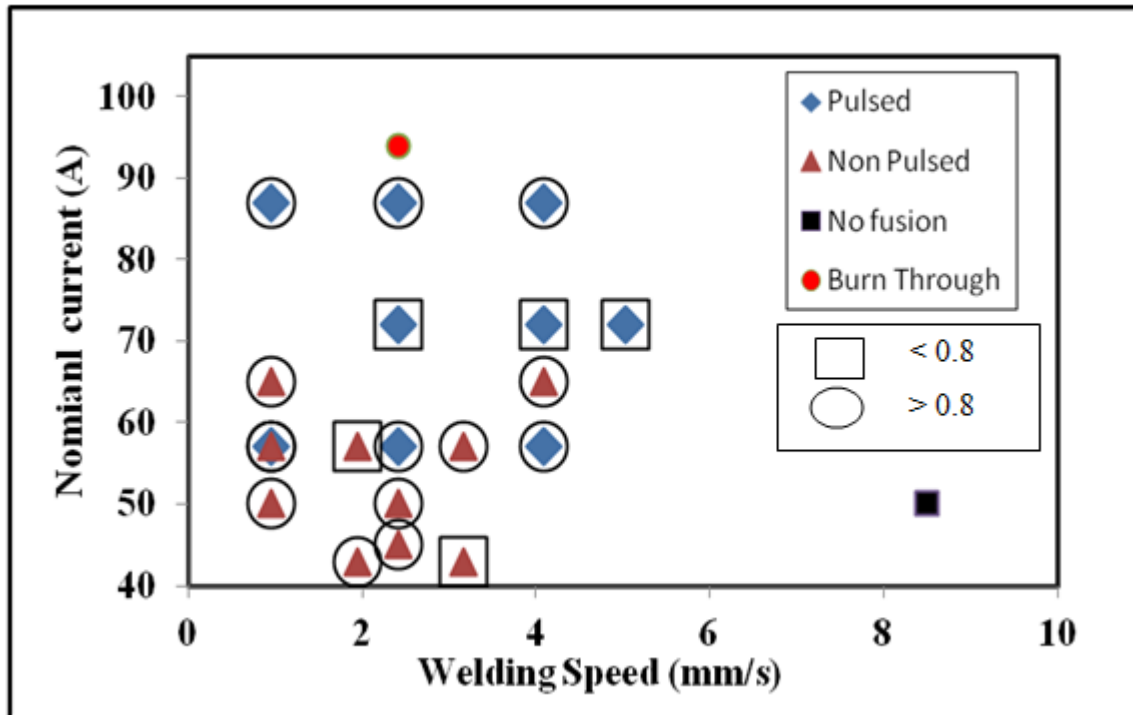
Figure 51: A map of the fraction basket-weave in the weld metal on the welding matrix.

7.4 Fraction basket-weave in weld metal and heat affected zone as a function of cooling rate

The calculated cooling rate of the welded joint ranged from 12°C/s to 480°C/s. During dilatometry, the cooling rate ranged from 11°C/s to 600°C/s. At these cooling rates investigated, an average of 0.80 basket-weave structure was observed. This microstructure is consistent with Holt[10] and Perez & Saggese[9] reported results at similar cooling rates as seen in Table 13. Basket-weave microstructure is commonly found in Zircaly-4 than in Zircaloy -2. Noting that the composition of Zircaloy -4 contains nickel, which is added for corrosion resistance purposes. Nickel may form SPP -Zr_2(Ni, Fe) which are nucleation sites for basket-weave structure as basket-weave can nucleate on a number of habit planes.

Table 13: Comparison of the transformation product of this work with published cooling rates, expressed as the cooling rate (in °C/s) that resulted in a specific structure, for zirconium 1.5%Sn

Transformation product	Holt[10] Zircaloy-4 Cooling rate (°C/s)	Perez& Saggese[9] Zircaloy-4 Cooling rate (°C/s)	Current study Zirconium 1.5%Sn (weld metal& HAZ) Cooling rate (°C/s)
Martensite	2000	≥1500	Cooling rate not used
Mixed structure of martensite and basket-weave	not reported	1500-600	Cooling rate not used
Basket-weave	200 - 20	600 - 10	Predominantly basket-weave 600-11
Intermediate basket-weave and parallel plate	not reported	10 - 2	Cooling rate not used
Parallel plate	not reported	2 - 0.5	Cooling rate not used
Lenticular	not reported	≤0.5	Cooling rate not used

Note [1]: For this study, the average fraction basket-weave structure in the weld metal was 0.80±0.10. The balance of the structure consisted of parallel-plate structure (see

Weld 7 basket-weave structure 95% confidence calculation:

The variance is given by,

$$\left(\frac{\sigma(P_p)^2}{P_p^2}\right) = \frac{1}{P_\alpha} \quad \text{Equation 1}$$

Therefore,

$$\sigma(P_p) = \frac{P_p}{\sqrt{P_\alpha}}$$

Where:

$\sigma 2$ is the variance

$P\alpha$ is the number of points counted in the basket-weave microstructure

Pp point fraction in the basket-weave microstructure

$$\sigma(P_p) = \frac{0.9}{\sqrt{90}}$$

$$\sigma(P_p) = 0.0942$$

The 95% confidence interval is given by,

95% confidence interval=1.96* $\sigma(P_p)$ Equation 2

95% confidence interval=1.96* 0.0942

95% confidence interval=0.19

Weld 7 grain size calculation:

The average of the grain size was determined as follows.

$$average = \frac{2x(200) + 67 + 9x(100) + 170 + 140 + 190}{15}$$

Average =125µm

The standard deviation was calculated as follows.

$$\text{Standard deviation} = \sqrt{\frac{\Sigma(x_i - x_{avg})^2}{(n-1)}}$$

$$\sqrt{\frac{(190-125)^2 + (140-125)^2 + 2x(200-125)^2 + (70-125)^2 + 9x(100-125)^2 + (173-125)^2}{14}}$$

$$\text{standard deviation} = 44 \ \mu m$$

where

The 95% confidence interval was determined as follows

$$\text{confidence interval} = x_{avg} \pm 1.96\left(\frac{44}{\sqrt{15}}\right)$$

and Table 9 for fraction basket-weave structure of weld metal and HAZ)

There are three main nucleation sites for an alpha plate i.e. prior beta grain, second phase particle and impurities. Figure 5 is consistent with microstructures seen in section 6.5.1 to 6.5.3 in that the parallel plate structure nucleates on prior beta grain boundaries and the basket-weave structure nucleates inside beta grains. A higher hardness is usually associated with presence of second phase particles[6]. An increase in hardness was not observed in this study (see section 7.3). Impurities elements such as carbon, phosphorus and silcon have low solubility in Zircaloy-2 and would form inclusions that would nucleate a basket-weave structure[5]. Thus, prior beta grain and inclusions are likely nucleation sites for basket-weave structure in this study.

7.4.1 Effect of pulsing

Table 14 shows the effect of pulsing on the microstructure. The pulsed microstructure at low heat input has finer microstructure and smaller grains compared to the non-pulsed microstructure heat low heat input as seen in Figure 42. The same effect is observed in the comparison of microstructures of pulsed and non pulsed at heat high heat input.

Table 14: The effect pulsing on the microstructure.

Current mode	Heat input (30-40J/mm)	Heat input (90 J/mm)
Pulsed		
Non Pulsed		

7.5 Weld metal and HAZ Hardness

Hardness was not a function of the heat input or the mode of current (see Figure 21 and Figure 22). Moreover, there was no significant difference between the hardness of the weld metal and HAZ for the given thickness investigated (see Table 11). The weld metal and HAZ hardness was measured at 174±3 HV and 170±3 HV respectively. In this study the base metal hardness was measured 184 HV which is lower than the hardness report by Etienne for Zircaloy-2 base metal (200 HV)[2]. For the welding parameters investigated in the welding matrix, the hardness did not vary, as seen in Figure 50. The weld metal structure was not sensitive to the cooling rate. The transformation product of prior β grain size on cooling was either parallel plate or basket-weave structure. Both parallel plate and basket-weave structures have a very fine grain size, much finer than the prior β grain size. It is expected that the fine grain size associated with both parallel and basket-weave structures dominated the hardness. As a consequence, the hardness was not sensitive β grain size. No martensite formed in the range of cooling rates investigated.

There was also no significant difference between the hardness of the good welds and that of the contaminated welds. The absence of a significant effect of gaseous contamination on the hardness of the welded joint was thought to be due to the fact that contamination by gaseous elements (hydrogen, nitrogen and oxygen) was not severe. The hardness of contaminated welds was similar to that of successful welds.

The hardness of the 19 successful welds was lower than the base metal but was not sensitive to cooling rate.

7.6 Transformation temperatures from α to β analysis using dilatometry

In this study, the transformation start, on heating, for all the samples were 807°C to 836°C and transformation end temperatures also on heating for all the samples were 1004°C to 1071°C as seen in Table 12 and Figure 45. On cooling, the transformation start temperatures for all samples were 838 to 934°C and transformation end temperatures were 801°C to 647°C. The calculated Δt_{9-6} reflects the time taken during the transformation range of temperatures on cooling and was considered appropriate. A peak temperature of 900°C therefore did not result in complete transformation to beta on heating. The use of a peak temperature of 1100°C was, therefore, justified.

7.7 Second phase particles

TEM work was done to investigate the second phase particles (SPPs). SPPs were found on the base material but not on the weld metal and HAZ. However, it cannot be conclusively said that there were no SPPs in the weld metal or the HAZ, though the Cr and Fe alloying content in the base material was probably too low to result in any significant precipitation during the welding. SPPs were reported to have been formed at cooling rates of between 7 and 300°C/s. No SPPs were found in the weld metal of weld 13 that has estimated cooling rate 25°C/s.

Hardness of Zircaloy alloys is a good indication of whether SPP are present, as they tend to make Zircaloy brittle and have a hardness higher than that of the base metal. In this study, as noted previously, the hardness of the weld metal and of the heat affected zone was consistently lower than

published values of 200HV[2] (in the order of 170±3HV – Table 11); the low hardness was consistent with the fact that SPPs were not observed.

8. Conclusions

- Exercising good shielding on both the backing plate and gas shielding produced visually good welds that were free of oxidation.

- For zirconium 1.5%Sn sheet with a thickness of 1.2 mm, welding above a current of 94 A caused burn through to occur and at a current of 35 A, arc initiation problems occurred. No fusion occurred at a welding speed above 5 mm/s.

- The 19 welds represented the feasible combination of welding speed and current that resulted in full-penetration autogenous welds in 1.2 mm thickness plate. Inside the operating window of welding speed and welding current, the hardness, grain size and percentage basket-weave did not change significantly with changes in welding parameters.

- The as-welded microstructure of the welds and dilatometry had, on average, a fraction of basket-weave structure of 0.80 at estimated cooling rates ranging from 600 to 11°C/s.

- There was no significant difference in hardness between weld metal and HAZ of low and high heat input done with pulsed and non-pulsed mode. The hardness was not sensitive to heat input and prior beta grain size for the welding matrix investigated at a thickness of 1.2 mm.

- The microstructure is finer and the grain sizes are smaller on the pulsed samples.

- There was no difference in hardness between contaminated and non-contaminated welds.

- A range of transformation start and transformation end temperatures were measured from the cooling rates investigated. On heating, the transformation start and transformation end temperatures were between 807°C and 1071°C. These temperatures were consistent with most published results. The transformation start and transformation end range on cooling was 801°C to 647°C. Thus, the use of cooling time from 900°C-600°C, Δt_{9-6} calculated for welds was therefore appropriate.

- The hardness and microstructure of the weld metal and the HAZ were similar.

The contribution of this study to the welding of zirconium 1.5%Sn is both on a practical welding and metallurgy of welding point of view. Although good shielding practises are essential, contamination of the weld by air did not adversely affect the mechanical properties. For the welding parameters considered at a thickness 1.2 mm, the grain size, microstructure and hardness are similar with changes in welding parameters. This study can inform the compilation of welding procedures for industrial applications.

References

[1] Oskarsson, M. 2000. Study on the Mechanisms for Corrosion and Hydriding of Zircaloy Doctoral Thesis, Royal Institute of Technology, Stockholm, Sweden.

[2] Ettienne, S undated. Welding and heat treatment in zirconium alloys practical aspects and recent examples of realizations available at:
https://www.atimetals.com/businesses/atispecialtyalloysandcomponents/Documents/Tech-Serv-Library/1997-Conf-Proceedings/1997015.pdf [2015, April 22].

[3] Northwood D, O. 1985. The Development and Applications of Zirconium Alloys *Material & Designs* Vol. 6 (2) pp 58-70.

[4] B352/B352M − 17, zirconium and zirconium alloy sheet, strip, and plate for nuclear application

[5] Massih, A, R. *et al*. 2003. Effect of quenching rate on the β-to-α phase transformation structure in zirconium alloy. *Journal of Nuclear Materials* Vol 322 (2003), pp138–151.

[6] Cotie, M, B.1982. The effect of second -phase particles on the corrosion and structure of Zircaloy-4 Masters Thesis, University Pretoria, Pretoria, RSA.

[7] Magwentshu, N & Pistorius P, G, H. 2015. Optimization of gas tungsten arc welding of Zircaloy-2 − results of preliminary study.*The Southern African Institute of Mining and Metallurgy Advanced Metals Initiative Nuclear Materials Development Network Conference.*

[8] Holt, R, A. 1969. The beta to alpha to phase transformation in Zircaloy-4. *Journal of Nuclear Materials*, Vol. 3, pp. 322-334.

[9] Perez, T, E & Saggese, M, E. 1982. Welding Structures in Gas Tungsten Arc-Welded Zircaloy-4 *Metallography*, Vol. 15, pp. 43-52.

[10] Chai, L, J. *et al.* 2012.Effect of cooling rate on beta to alpha transformation during quenching of Zr0.85 Sn-0.4 Nb-0.4 Fe-0.1 − Cr 0.05 Cu alloy. *Science China*, Vol 55 (10), pp.2960-2964.

[11] Griffiths, M, Gilbert, R, W and Cheadle, B, A. 1985. Formation, growth and precipitates in zircaloy - 2 and -4. Metallurgical Engineering Branch, Chalk River Nuclear laboratories, Chalk River, Ontario, Canada.

[12] Ahmad, M, *et al.* 1997. Microstructural study of two locally prepared Zircaloy-4, Nuclear Material Division. Pakistan- Technical report. Radiation Damage Group,Nuclear Physics Division *Institute of Nuclear Science & Technology*, Islamabad.

[13] Toffolon-Masclet, C, Guilbert, T and Brachet, J, C. 2007. Study of secondary intermetallic phase precipitation/dissolution in Zr alloys by high temperature–high sensitivity calorimetry. *Journal of Nuclear Materials.* Vol. 372 (2008), pp. 367–378.

[14] Saibaba, N, *et al.* 2010. Microstructural studies of heat treated treated Zr 2.5 Nb alloy for pressure tube application pressure tube application-Technical report. Bhabha atomic research centre, Mumbia, India.

[15] Lustman, B; Kerze, F, 1955. The metallurgy of zirconium. New York: McGraw- Hill series.

[16] Skinner, G, B & Johnston H, L.1953. Thermal expansion of zirconium between 200K and 1600K. *Journal of chemical physics*, Vol.21, pp. 8.

[17] SANS 15614-5:2008 ISO 15614-5:2004. South African National Standard. Specification and qualification of welding procedures for metallic materials — Welding procedure test — Part 5: Arc welding of titanium, zirconium and their alloys.

[18] Olson, D.L, Siewart T.A, Liu, S and Edwards G.R., editors, 1993. ASM Handbook Vol.6 Welding, Brazing and Soldering.

[19] Bangaru, N, R, V. 1985. An investigation of the microstructures heat treated Zircaloys -*4*. *Journal of Nuclear Materials,* Vol. 131, pp. 260-290.

[20] Vander Voort, G, F. 1984. Metallography principles and practice, New York: McGraw- Hill series.

[21] Shaaban, H,I, Hammad, F.H, Baron J,L. 1977. Investigation of diffusion bonding between Zircaloy-4 and 304. stainless steel. *Journal of Nuclear Materials,* Vol. 71, pp. 277-285.

[22] Ahmad, M, *et al.* 2001. Hardness and microstructural studies of electron beam welded joints of Zircaloy-4 and stainless steel. *Journal of Nuclear Materials,* Vol. 301, pp.118–121.

[23] Baek, J, H & Jeong Y, H. 2002. Depletion of Fe and Cr within precipitates during Zircaloy-4 oxidation .*Journal of Nuclear Materials*, Vol. 304, pp.107–116.

[24] Ahmad, M. *et al*. 2005. Microstructure and non-equilibrium phases in electron beam-welded joints of Al–Fe–Ce and Zircaloy-4. *Journal of Nuclear Materials*, Vol. 34, pp164–168.

[25] Ahmad, M *et al*. 2006. Characterization of electron beam modified surface of Zircaloy-4 *Journal of Alloys and Compounds*, Vol 426, pp.176–179.

[26] Underwood, E, E, 1970. Quantitative Stereology. Massachusetts: Addison Wesley.

[27] Easterling, K. 1992, Introduction to the Physical Metallurgy of Welding. Oxford : Butterworth-Heinemann.

[28] Murabayashi, M, Tanaka, S & Takahashi, Y, 1975, Thermal conductivity and heat capacity of Zircaloy- 2, and unalloyed -4 Zirconium, *Journal of Nuclear Science and Technology*, Vol. 12(10), pp. 661-662.

[29]Atkins, M, 1980. Atlas of continuous cooling transformation diagrams foe engineering steels Ohio: American society for metals.

Appendix A

Table14: Summary of welding parameter and calculated welding data

Weld ID	Speed (mm/s)	welding current (A)	Welding mode	Welding Voltage (V)	Electrical Heat Input (kJ/mm) $(q/\upsilon)_e$	Avg width of weld bead (mm)	Rosenthal calculated Heat input (J/mm)	Estimated Arc efficiency	$\Delta t_{9\text{-}6}$ (s)	Cooling Rate (°C/s)
1	0.95	50	DC	9	0.48	5.85	50	0.11	8.4	36
2	1.94	57	DC	9	0.26	6.625	60	0.23	10.7	28
3	4.08	87	Pulsed	9	0.15	6.85	60	0.44	11.5	26
4	4.08	72	Pulsed	10	0.13	3.95	40	0.27	3.8	79
5	2.42	87	Pulsed	10	0.27	8.95	80	0.30	19.6	15
6	0.95	57	Pulsed	10	0.46	5.8	50	0.12	8.2	37
7	3.16	57	DC	9	0.16	4.25	40	0.24	4.4	68
8	4.08	57	Pulsed	9	0.10	1.6	10	0.16	0.6	480
9	1.94	43	DC	9	0.20	4.15	40	0.19	4.2	71
10	2.42	45	DC	10	0.19	3.85	40	0.19	3.6	83
11	2.42	50	DC	10	0.21	7.75	70	0.35	14.7	20
12	0.95	57	DC	9	0.54	6.65	60	0.11	10.8	28
13	2.42	72	Pulsed	9	0.20	6.95	60	0.32	11.8	25
14	5.03	72	Pulsed	9	0.10	1.6	10	0.15	0.6	480
15	2.42	57	Pulsed	9	0.16	3.2	30	0.18	2.5	120
16	2.42	87	Pulsed	10	0.27	9.2	90	0.31	20.7	15
17	0.95	65	DC	10	0.69	10	90	0.14	24.4	12
18	4.08	65	DC	10	0.16	5	50	0.29	6.1	49
19	3.16	43	DC	10	0.14	1.6	10	0.11	0.6	480

Table15: Summary of welding parameter of contaminated welds

	Contaminated weld 1	Contaminated weld 2	Contaminated weld 3	Contaminated weld 4	Contaminated weld 5
Contamination colour	light blue	light yellow	blue	blue	dark blue
Current mode	non-pulsed	pulsed	non-pulsed	pulsed	non-pulsed
Current	57A	50 A	50 A	94 A	50 A
Speed	0.94 mm/s	2.4 mm/s	2.4 mm/s	2.4 mm/s	2.4 mm/s
Voltage	9 V	9 V	10 V	10 V	10 V